Article

SOURCE DATA | TRANSPARENT PROCESS | OPEN ACCESS

THE EMBO JOURNAL

AATF/Che-1 localizes to paraspeckles and suppresses R-loops accumulation and interferon activation in Multiple Myeloma

Tiziana Bruno[1,†], Giacomo Corleone[1,†], Valeria Catena[1,†], Clelia Cortile[1], Francesca De Nicola[1], Francesca Fabretti[2,3], Svitlana Gumenyuk[4], Francesco Pisani[4], Andrea Mengarelli[4], Claudio Passananti[5] & Maurizio Fanciulli[1,*]

Abstract

Several kinds of stress promote the formation of three-stranded RNA:DNA hybrids called R-loops. Insufficient clearance of these structures promotes genomic instability and DNA damage, which ultimately contribute to the establishment of cancer phenotypes. Paraspeckle assemblies participate in R-loop resolution and preserve genome stability, however, the main determinants of this mechanism are still unknown. This study finds that in Multiple Myeloma (MM), AATF/Che-1 (Che-1), an RNA-binding protein fundamental to transcription regulation, interacts with paraspeckles via the lncRNA NEAT1_2 (NEAT1) and directly localizes on R-loops. We systematically show that depletion of Che-1 produces a marked accumulation of RNA:DNA hybrids. We provide evidence that such failure to resolve R-loops causes sustained activation of a systemic inflammatory response characterized by an interferon (IFN) gene expression signature. Furthermore, elevated levels of R-loops and of mRNA for paraspeckle genes in patient cells are linearly correlated with Multiple Myeloma progression. Moreover, increased interferon gene expression signature in patients is associated with markedly poor prognosis. Taken together, our study indicates that Che-1/NEAT1 cooperation prevents excessive inflammatory signaling in Multiple Myeloma by facilitating the clearance of R-loops. Further studies on different cancer types are needed to test if this mechanism is ubiquitously conserved and fundamental for cell homeostasis.

Keywords AATF/Che-1; multiple myeloma; NEAT1; R-loops

Subject Categories Cancer; DNA Replication, Recombination & Repair; RNA Biology

DOI 10.15252/embj.2021109711 | Received 14 September 2021 | Revised 6 July 2022 | Accepted 14 July 2022 | Published online 5 August 2022

The EMBO Journal (2022) 41: e109711

Introduction

During transcription, the nascent RNA binds with the template strand of DNA, removing the complementary DNA strand, thus leading to the formation of RNA:DNA hybrids. These three-stranded nucleic acid structures, composed of RNA:DNA hybrids and the associated nontemplate single-stranded DNA are called R-loops (Santos-Pereira & Aguilera, 2015; Garcia-Muse & Aguilera, 2019). Failure to control the generation of these structures can lead to transcription blockage and the generation of DNA damage and genomic instability. Numerous mechanisms are involved in the correct regulation of R-loops, and their accumulation appears to be related to numerous neurodegenerative and oncological pathologies (Groh & Gromak, 2014; Santos-Pereira & Aguilera, 2015; Belotserkovskii *et al*, 2018; Garcia-Muse & Aguilera, 2019).

Multiple Myeloma (MM) is a hematological malignancy characterized by the uncontrolled proliferation of transformed plasma cells in the bone marrow and the overproduction of immunoglobulins (Kumar *et al*, 2017). This neoplasm is characterized by a high frequency of chromosomal aberrations, genomic instability (Manier *et al*, 2016, 2017; Neuse *et al*, 2020), and intrinsic DNA damage (Cottini *et al*, 2015). Despite continuing advances in the treatment of this disease, MM remains an incurable disease (Kumar *et al*, 2017) and understanding the molecular mechanism underlying the progression and identification of key factors driving the aggressiveness is of fundamental importance.

Recent studies demonstrated that the protein Che-1/AATF (Che-1) promote MM transformation and progression by affecting chromatin accessibility and global transcription (Desantis *et al*, 2015; Bruno *et al*, 2020). Che-1 is an RNA polymerase (RNA Pol) II-interacting protein highly conserved during evolution (Fanciulli *et al*, 2000). During the last 20 years, it has been demonstrated that

1 SAFU Laboratory, Department of Research, Advanced Diagnostics, and Technological Innovation, Translational Research Area, IRCCS Regina Elena National Cancer Institute, Rome, Italy
2 Department II of Internal Medicine and Center for Molecular Medicine Cologne, Faculty of Medicine and University Hospital of Cologne, University of Cologne, Cologne, Germany
3 Cologne Excellence Cluster on Cellular Stress Responses in Aging-Associated Diseases (CECAD), University of Cologne, Cologne, Germany
4 Hematology Unit, IRCCS Regina Elena National Cancer Institute, Rome, Italy
5 Department of Molecular Medicine, CNR-Institute of Molecular Biology and Pathology, Sapienza University of Rome, Rome, Italy
*Corresponding author. Tel: +3906 5266 2800; Fax: +3906 5266 2980; E-mail: maurizio.fanciulli@ifo.it
†These authors contributed equally to this work

© 2022 The Authors. Published under the terms of the CC BY NC ND 4.0 license.

Che-1 is involved in many fundamental cellular processes, such as transcriptional regulation, cell-cycle and apoptosis control, cellular response to DNA damage and stress, and ultimately progression of many types of cancer (Iezzi & Fanciulli, 2015; Folgiero *et al*, 2018; Jing *et al*, 2018; Welcker *et al*, 2018; Kumar *et al*, 2019).

Accumulating evidence indicates that transcription is regulated by the action of paraspeckles, nuclear bodies identified in the interchromatin space of the cells (Fox & Lamond, 2010; Fox *et al*, 2018). These structures are composed of specific RNA and at least 40 different proteins, essentially RNA-binding proteins (RBP) expressed ubiquitously (Fox *et al*, 2018). The formation of the paraspeckle is mediated by the architectural long noncoding RNA (lncRNA) NEAT1_2 (NEAT1) which acts as a scaffold for the assembly of the components of this organelle (Clemson *et al*, 2009). In addition to NEAT1, numerous RBPs such as NONO, SFPQ, FUS, or RBM14 are essential for the formation and maintenance of paraspeckles (Yamazaki & Hirose, 2015). These organelles dynamically control the shuttling of specific proteins and mRNAs between this compartment and the nucleoplasm. Nevertheless, NEAT1 interacts with chromatin and localizes at transcription start sites (TSS) of active genes, leading to hypothesize a direct involvement of this lncRNA on transcription (West *et al*, 2014).

In this study, we show that Che-1 interacts with numerous paraspeckle components, in particular with lncRNA NEAT1. Che-1 and NEAT1 colocalize on the DNA, and NEAT1 modulates the presence of Che-1 on chromatin, regulating the formation of R-loops. Depletion of Che-1 or NEAT1 produces an accumulation of these structures and activation of inflammatory pathway. Notably, we demonstrate that hybrid structures increase in MM patient cells and observe a linear relationship between the progression of MM and the expression of paraspeckle and IFN response genes. Finally, our findings suggest a marked worse prognosis in MM patients showing elevated activation of IFN response.

Results

Che-1 interacts with paraspeckle components

Che-1 is a nuclear protein involved in transcription regulation and cell proliferation of MM. To shed more light on its role in this disease, we performed co-immunoprecipitation experiments coupled with a mass-spectrometry analysis (Fig 1A). Mass spectrometry revealed that ~600 proteins were significantly enriched in Che-1 precipitates. As expected from its role in ribosomal RNA maturation, the Che-1 interactome contains numerous proteins involved in pre-rRNA processing (Bammert *et al*, 2016; Liu *et al*, 2018; Kaiser *et al*, 2019) and several ribosomal proteins (Kaiser *et al*, 2019). Notably, among other proteins interacting with Che-1, we identified many essential components of the paraspeckle (Fox *et al*, 2018; Fig 1B; Dataset EV1), and these results were further confirmed by a previous mass-spectrometry analysis performed in HeLa cells (Kaiser *et al*, 2019; Appendix Fig S1A), thus suggesting a conserved role of Che-1/paraspeckles protein interaction in multiple model systems. To validate these results, we evaluated the binding of Che-1 to two important components of the paraspeckle, NONO and SFPQ. Reciprocal endogenous co-immunoprecipitations (co-IP) showed a strong interaction of Che-1 with both these proteins mediated at least in part by RNA, as treatment with RNase A affected their binding (Fig 1C) and immunofluorescence analyses showed a co-localization of Che-1 with both SFPQ and NONO (Fig EV1A and Appendix Fig S1B). Moreover, proximity ligation assays (PLA) confirmed these results, showing discrete spots by fluorescence microscopy in Kms27 MM cells (Fig EV1B). To investigate a direct binding of Che-1 with NEAT1, we integrated in our framework data from the largest database of RBP binding to date (Van Nostrand *et al*, 2020). We leveraged our ability to infer RBPs/NEAT1 binding to date in immortalized leukemia and liver hepatocellular carcinoma cell lines (K562, HepG2), which confirmed the binding of Che-1 occur to NEAT1 5′ and 3′ functional domains (Fig EV1C and Appendix Fig S1C). In line with the model proposed by Yamazaki *et al* (2018), three fundamental components of the paraspeckle core, NONO, SFPQ, and FUS contribute to paraspeckle assembly and stabilization by binding to both the middle and peripheral domains overlapping with Che-1 signal.

RNA immunoprecipitation (RIP) assays performed in Kms27 and RPMI8226 MM cells demonstrated that Che-1 can bind both NEAT1_1 and NEAT1_2 (Fig 1D; Appendix Fig S1D), and immunofluorescence experiments showed NEAT1/Che-1 and NEAT1/NONO colocalizations in these cells (Figs 1E and EV1D). Several studies have shown Che-1 as a nucleolar protein (Ferraris *et al*, 2012; Bammert *et al*, 2016; Pineiro *et al*, 2018; Kaiser *et al*, 2019; Sorino *et al*, 2020). Thus, we evaluated whether NEAT1 was also present in these structures. As shown in Fig EV1E and F, both NEAT1 and SFPQ were detected to colocalize with fibrillarin, confirming the presence of these proteins in the nucleolus. Finally, we tested whether NEAT1 mediates the interactions of Che-1 with NONO and SFPQ. Immunoprecipitations assays demonstrated that NEAT1 depletion strongly reduces Che-1/SFPQ interaction but not NONO/SFPQ heterodimer formation (Fig 1F), confirming the results showed in Fig 1C. Overall, our data support the hypothesis that Che-1 is a component of paraspeckles by interacting directly with NEAT1 in the nucleolus.

Che-1 and NEAT1 colocalize on the DNA

Previous studies identified the lncRNA NEAT1 as an essential structural determinant of paraspeckles. It has been demonstrated that these structures regulate gene transcription in response to different types of stress by sequestrating specific RNAs and proteins within them (Hirose *et al*, 2014; Fox *et al*, 2018). Moreover, NEAT1 is detectable bound at the DNA of nucleosome-depleted regions associated to active transcription sites (West *et al*, 2014). To investigate the potential co-binding affinity of NEAT1 and Che-1 at DNA, we first identified NEAT1-binding site with chromatin isolation by RNA purification (ChIRP-seq) and Che-1 binding with chromatin immunoprecipitation (ChIP-seq) experiments in Kms27 MM cells and developed computational signal dissection approach to define evidence of co-binding at same loci. Our approach relied on the identification at high resolution of NEAT1 and Che-1-binding sites followed by a quantification of both signals at potential ~92 k Transcription Starting Sites (TSS). ChIRP-seq and ChIP-seq signals were independently normalized, ranked for Jaccard similarity index. Finally, signals we assigned to 3 groups accordingly to mathematical evidence: NEAT1/Che-1 co-binding, only Che-1 and only NEAT1 (Fig 2A).

© 2022 The Authors

ChIRP-seq enriched at 19,1369 regions while Che-1 ChIP-seq at 41,061 binding sites (Appendix Fig S2A). Enriched regions were classified according to their genomic position. Che-1 was more prone to bind downstream the promoter (TTS, −100 bp to +1 kb genomic window) while NEAT1 at gene bodies (Fig 2B). Interestingly, ~30% of Che-1 and NEAT1 sites bound at noncoding regions thus suggesting a functional role for those sites which could be further investigated. These data agree with NEAT1 and Che-1 being key determinants of gene transcription regulation. To gain insights into the binding at the TSSs we leveraged the genomic annotation obtained from Ensembl GRCh37 by surveying the signal at 92,226 sites. We identified those sites showing Che-1/NEAT1 co-binding (N = 14,654), Che-1 only sites (N = 16,152) and NEAT1 only sites (N = 10,395) (Fig 2C). Most co-binding sites (87% of the totality) were occurring at promoter proximity (Distance to promoter TSS between 0–50 Kb) (Fig 2D). Ontologies and pathways analysis for the genes associated to those sites showed highly significant enrichments for active transcription and metabolic process (Fig 2E). These data prompted us to investigate whether Che-1/NEAT1 co-binding was occurred at open chromatin sites. Accordingly, we profiled H3K27ac ChIP-seq data of Kms27 MM cell lines and integrated the signal with NEAT1 and Che-1 sites (Fig 2F). Strikingly 47% of co-binding sites was overlapping with H3K27ac-marked regions while Che-1 only and NEAT1 only sites were occurring at active sites at 36

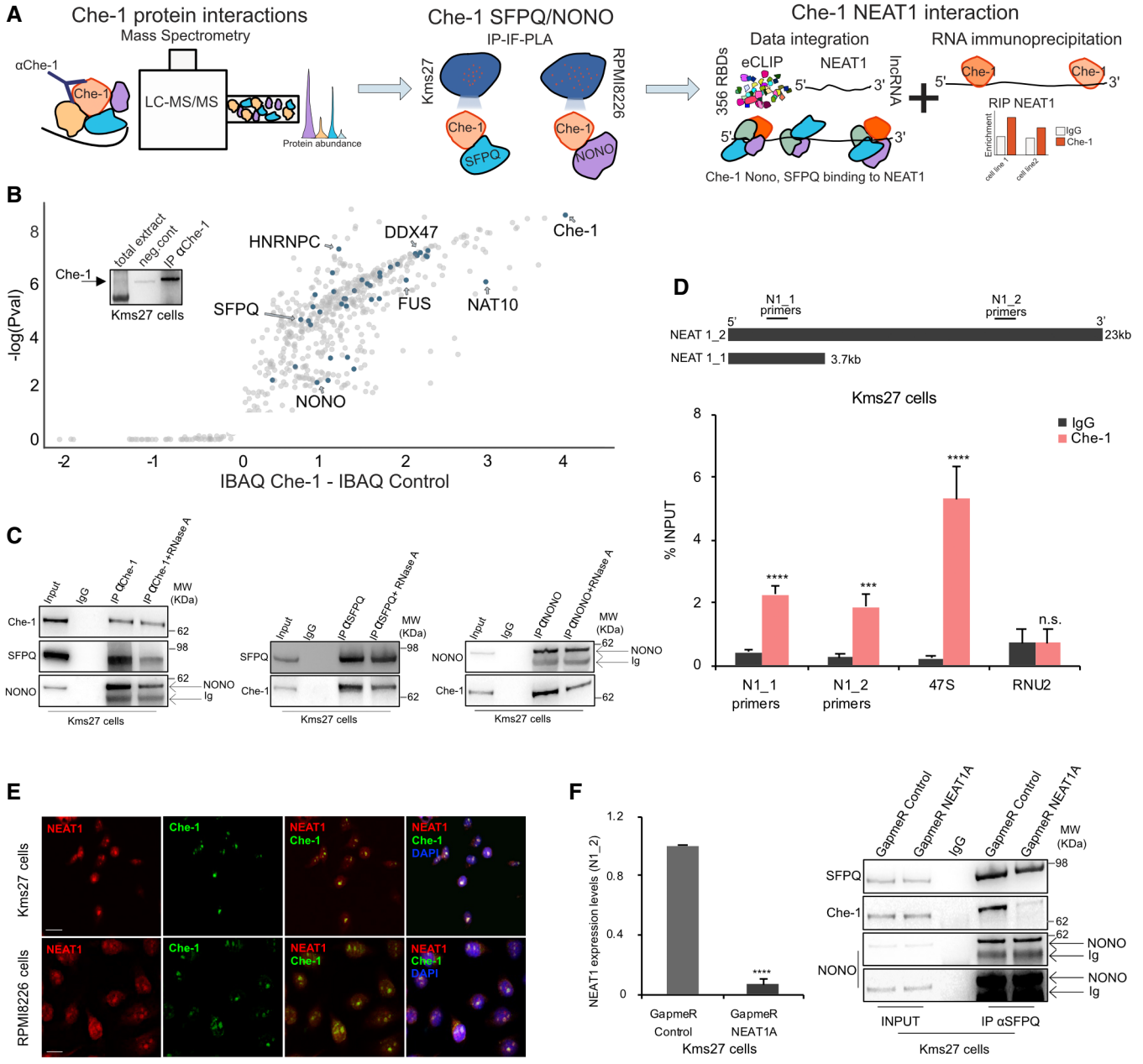

Figure 1.

Figure 1. Che-1 interacts with paraspeckle components.

A Experimental and computational workflow followed to test the relationship between Che-1 and paraspeckle components. *(Left)* Mass spectrometry analysis was performed to identify Che-1 interactome followed by: *(Middle)* Che-1 SFPQ/NONO co-immunoprecipitation (Co-IP) immunofluorescence (IF) and Proximity ligation assay (PLA) to evaluate physical interaction. (*Right)* Then eCLIP data of 356 RNA Binding Protein in K562 cell line was evaluated at NEAT1 locus followed by Che-1 RNA immunoprecipitation (RIP) and co-localization in KMS27 and RPMI8226 Multiple Myeloma (MM) cell lines.

B Scatter Plot of mass spectrometry assay. Dots depict protein intensity (IBAQ) and relative significance obtained from mass spectrometry assay. *X*-axis: Difference of Che-1 intensity versus IP control; on the *y*-axis are the corresponding −log10 *P*-values. Significant Che-1 interacting proteins relevant in this study are represented in blue. For a complete list of all significant Che-1 interactors, please refer to Dataset EV1.

C Nuclear extracts from Kms27 MM cells treated or not with RNase A were subjected to immunoprecipitation with the indicated antibodies (abs) and analyzed by western blot (WB) with the indicated abs. Input corresponds to 5% of the total extract used for immunoprecipitation.

D *(Top)* qRT-PCR approach described in the schematic representation. *(Bottom)* RIP-qPCR analysis with anti-Che-1 specific antibody or control rabbit IgG of Kms27 MM cells. Data are expressed as percent of Input. Error bars represent the standard error of three different biological experiments performed in technical duplicate (Two Tailed *t*-test ***$P < 0.005$, ****$P < 0.001$, n.s. = not significant).

E Colocalization assays in Kms27 and RPMI8226 MM cell lines by combining In Situ Hybridization (FISH) staining of NEAT1 (Stellaris) with immunofluorescence of Che-1. Scale bar 10 μm.

F (*Left*) RT-qPCR analysis of NEAT1 expression levels in Kms27 MM cells transiently transfected with LNA GapmeR NEAT1A or GapmeR Control oligonucleotides. Values were normalized to Actin expression. Error bars represent the standard error of three different biological experiments performed in technical duplicate (Two Tailed *t*-test ****$P < 0.001$). (*Right*) Nuclear extracts from KMS27 MM cells were immunoprecipitated with the indicated abs and analyzed by WB with the indicated abs.

Source data are available online for this figure.

and 11%, respectively (Appendix Fig S2B). Taken together, these data strongly support a potential regulatory role for Che-1 in occurrence with NEAT1 at active genes.

NEAT1 is required for recruiting Che-1 onto the DNA

Next, we investigated whether the Che-1/NEAT1 interaction could affect the localization of Che-1 in the nucleus. NEAT1 depletion by two specific antisense LNA GapmeRs in Kms27 MM cells (Fig 3A) did not affect Che-1, NONO, or SFPQ expression (Fig 3B) but produced a dispersion of NONO and SFPQ into the nucleus (Fig EV2A) and a cytoplasmatic Che-1 re-localization (Figs 3C and EV2B). Similar results were obtained in another MM cell line RPMI8226 (Appendix Fig. S3A–C). To confirm these results, we probed the presence of Che-1 in the various cellular components. As shown in Fig 3D, the downregulation of NEAT1 produced an accumulation of Che-1 in the cytoplasm and in the nucleoplasm, together with a concomitant decrease in the total chromatin fraction. Consistent with these findings, Che-1 ChIP-seq analysis revealed a marked global decrease of Che-1 occupancy at the Che-1/NEAT1 colocalization sites in NEAT1-depleted cells (Fig 3E). Remarkably, NEAT1 depletion in MM cells recapitulated the effects of Che-1 downregulation (Bruno *et al*, 2020), with a reduction in cell proliferation and global RNA synthesis and a significant downregulation of several genes involved in MM pathogenesis, such as *IRF4* or *MMSET* (Bruno *et al*, 2020) (Appendix Fig. S3D–F). To further characterize the Che-1/NEAT1 interaction, we evaluated the effects of Che-1 downregulation on the presence of NEAT1 onto the DNA. As shown in Appendix Fig S3G, Che-1 depletion produced a slight reduction of NEAT1 expression (about 20%). Fluorescence In Situ Hybridization (FISH) analysis performed in Kms27 MM cells showed that Che-1 depletion does not affect NEAT1 localization (Fig 3F). Moreover, ChIRP-seq analysis performed in Che-1-depleted Kms27 MM cells showed that only a marginal fraction of NEAT1 peaks were affected by Che-1 depletion (Figs 3G and EV2C). Indeed, approximately 90% of Che-1 and NEAT1 colocalizing sites, maintained similar NEAT1-enrichment in response to Che-1 downregulation. Taken together, our results show that NEAT1 is required for recruiting Che-1 onto the DNA, whereas NEAT1 binding on DNA is not dependent to Che-1 occurrence.

Che-1 and NEAT1 prevent RNA:DNA hybrids formation during transcription

While these analyses supported a strong interplay between NEAT1 and Che-1, the functional significance of this interaction was unknown. Recently, a mass spectrometry study identified the R-loops interactome in human cells, dynamic structures which contribute to gene regulation in health and disease (Cristini *et al*, 2018). Interestingly, RNA:DNA hybrids and Che-1 interactomes shared a large percentage of proteins suggesting that Che-1 and paraspeckle proteins could be present on the RNA:DNA hybrids in MM cells (Fig 4A *Left*). In addition, Wu *et al* (2021) recently performed stringent purification of proteins associated with R-loops in mouse embryonic stem cells, demonstrating the presence of numerous nucleolar proteins, including Che-1, among the R-loop-associated proteins (Fig 4A *Right*). Thus, co-IP experiments were performed with Kms27 and RPMI8226 MM cells' chromatin extracts by using the S9.6 antibody, which recognizes RNA:DNA hybrids (Boguslawski *et al*, 1986). These experiments showed that Che-1, NONO, and SFPQ bind RNA:DNA hybrids, and that these interactions are specific, since they disappeared after RNase H treatment (Fig 4B). Consistent with these results, PLA experiments revealed the presence of Che-1 on RNA:DNA hybrids (Fig 4C). To assess whether NEAT1 was also present on RNA:DNA hybrids, we performed RIP experiments using the S9.6 antibody. As shown in Fig EV3A, NEAT1 was found on these hybrids in both Kms27 and RPMI8226 MM cells. Notably, the presence of Che-1, SFPQ, and NONO on the RNA:DNA hybrids appeared to be mediated by NEAT1, since the depletion of this lncRNA strongly reduced the interaction between these three proteins and RNA:DNA hybrids (Fig 4D).

To investigate the role of Che-1 in R-loops metabolism, we depleted Che-1 expression in MM cells by two specific siRNA oligonucleotides (siChe-1A and siChe-1B). As shown in Fig. 4E and F, and Appendix S4A and B, Che-1 down-regulation produced a strong accumulation of R-loops in these cells, which disappeared

 © 2022 The Authors

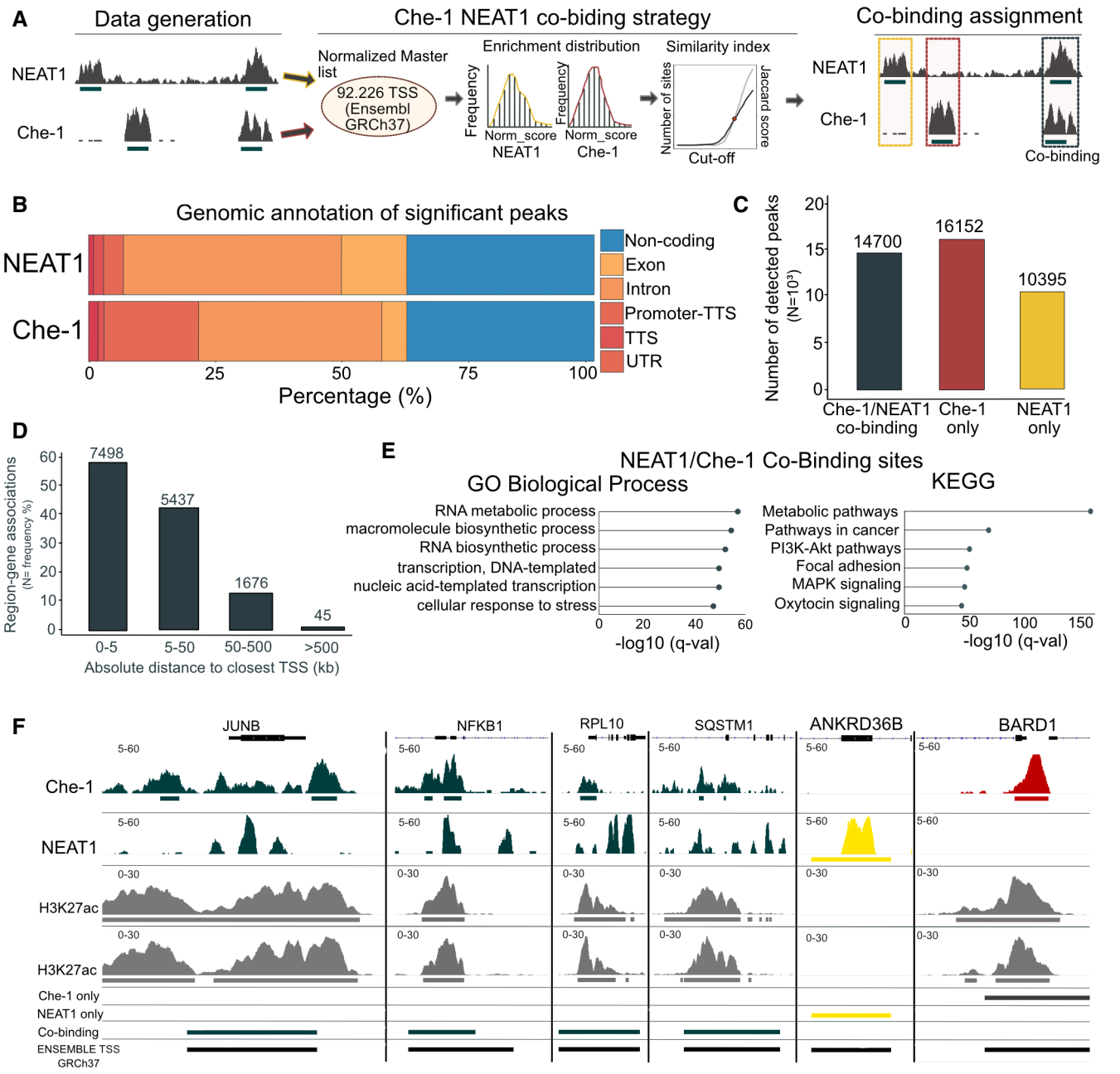

Figure 2. Che-1 and NEAT1 colocalize on the DNA.

A Experimental and computational workflows developed to identify NEAT1/Che-1 co-binding sites in MM Kms27 cells. ChIRP-seq and ChIP-seq were used to identify NEAT1 and Che-1-biding sites, respectively. Then, normalized read enrichment of both experiments was assessed at 92,226 transcription starting sites (coordinates from Ensembl GRCh37). Peaks were classified using an iterative approach of selection and assignment based on Jaccard scoring (*Middle*). Finally, peaks were classified into only NEAT1, only Che, Che-1/NEAT1 co-binding.

B Genomic annotation of significant peaks from the NEAT1 ChIRP-seq (*Top bar*) and Che-1 ChIP-seq (*Bottom bar*) experiments. Peaks were classified among six categories: Noncoding, Exon, Intron, Promoter-TTS, TTS, UTR according to Homer annotation tool. Each category is shown with a different color. The percentage of classified peaks for each category is shown as experiment-specific percentage (*x*-axis).

C Bar diagram showing the number of peaks shared between NEAT1/Che-1 (black), Che-1 only, (red), NEAT1 only (yellow). The peak number is shown at the top of each bar.

D Bar diagram showing the relative distance of each Che-1/NEAT1 co-binding peak to the closest gene. Distance is calculated as absolute value and is expressed in kilobase. The number of peaks per category at the top of each bar. Bar height represents the proportion of peaks included in each category to the total (N = 14,654).

E Gene Ontology (*Left*) and KEGG enrichment pathways analysis (*Right*) of Che-1/NEAT1 co-binding sites. The top 6 enriched terms are shown. Only ontology terms significant by both the binomial and hypergeometric tests using the multiple hypothesis correction false discovery rate are considered in this analysis. The represented q-value (*x*-axis) corresponds to the hypergeometric test.

F Che-1 ChIP-seq, NEAT1 ChIRP, H3K27ac ChIP-seq, Che-1 only, NEAT1 only, Co-Binding sites, ENSEMBLE TSS annotation (From Top to Bottom) signals at selected genomic loci (Genome reference: GRCh37). Color scheme: RED: Che-1 only signals; Yellow: NEAT1 only signals; Dark Green: co-binding sites.

© 2022 The Authors

after treatment by RNase H. Notably, Che-1 depletion effects obtained from a third oligonucleotide targeting the 3'UTR region of Che-1, were complemented by the overexpression of Che-1 (Fig EV3B).

Since it has been shown that the use of the S9.6 antibody in immunofluorescence produces numerous artifacts (Smolka *et al*, 2021), we transfected Kms27 MM cells with Cy5-labeled RNA:DNA hybrids, finding Cy5-associated S9.6 foci in control cells and in those treated with RNase T1 and RNase III, but not in cells treated with RNase H, confirming that the latter enzyme specifically degrades RNA:DNA hybrids (Fig EV3C). Then, Che-1-depleted Kms27 MM cells were treated with these three RNases, observing the disappearance of the nuclear R-loops only in the cells treated with RNase H (Fig EV3D). These findings were further confirmed by

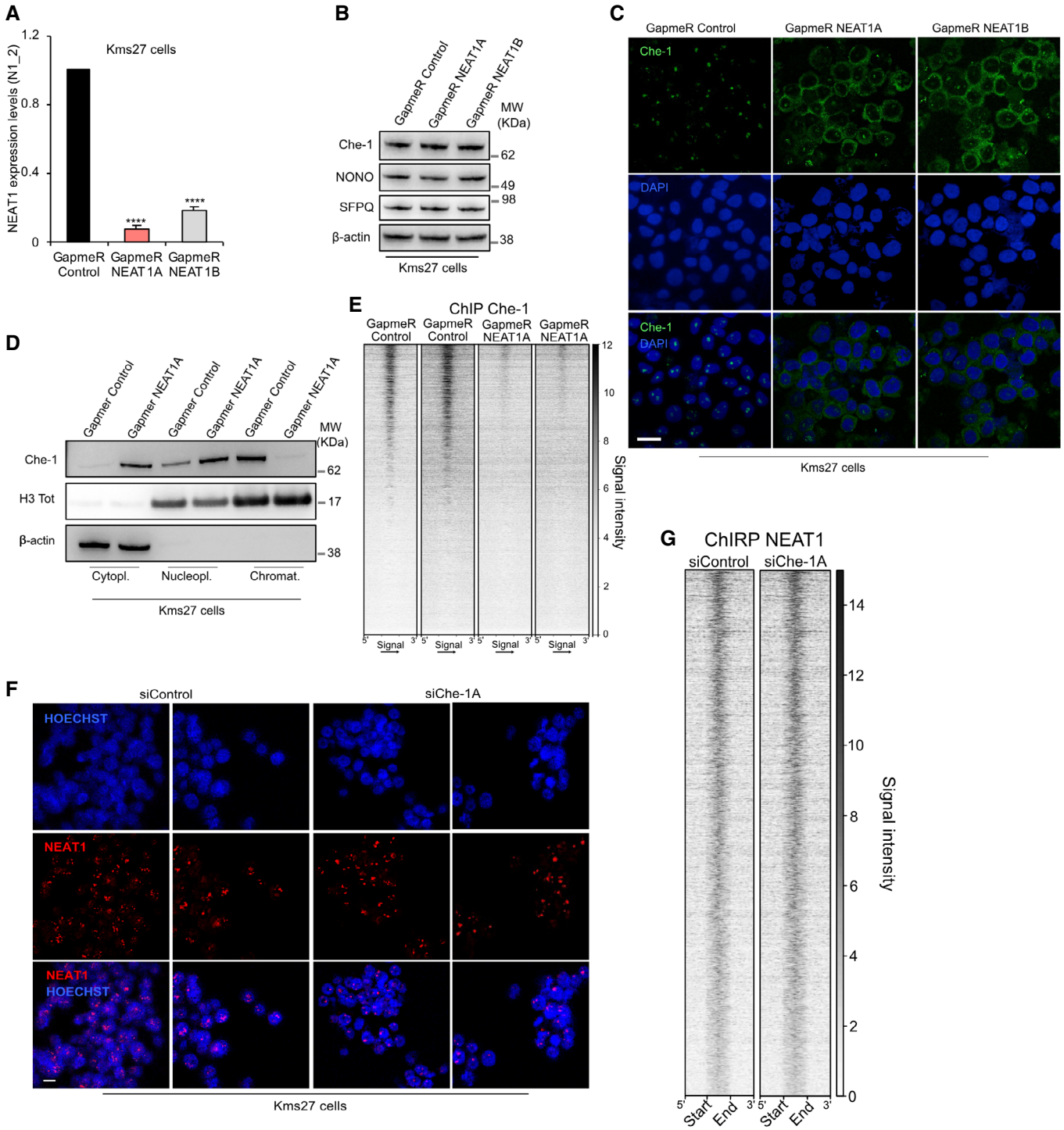

Figure 3.

© 2022 The Authors

Figure 3. NEAT1 is required for recruiting Che-1 onto the DNA.

A Quantitative RT-PCR (RT-qPCR) of Kms27 MM cells transiently transfected with two different LNA GapmeR NEAT1 or GapmeR Control oligonucleotides. Values were normalized to Actin expression. Error bars represent the standard error of three different experiments performed in duplicate (Two Tailed *t*-test ****$P < 0.001$).

B WB analysis with indicated abs of total extracts from Kms27 MM cells transiently transfected as in A.

C Representative confocal images of Kms27 MM cells transiently transfected with LNA GapmeR NEAT1A, GapmeR NEAT1B, or GapmeR Control oligonucleotides and immunostained with anti-Che-1 antibody. Scale bar 10 μm.

D Isolated cell compartments from Kms27 MM cells transfected with LNA GapmeR NEAT1A or GapmeR Control oligonucleotides, were subjected to WB with the indicated abs.

E Che-1 ChIP-seq signal intensity of LNA GapmeR NEAT1A (2 replicates on right) and GapmeR Control (2 replicates on left) and at co-localizing Che-1/NEAT1 sites ($N = 14{,}654$ sites). Signal intensity from 1 (weak) to 12 (strongest).

F FISH images of Kms27 MM cells depleted or not for Che-1 expression (siChe-1A) labeled with Hoechst (cell nuclei) and Quasar 670 (NEAT1 RNA). Scale bar 10 μm.

G NEAT1 ChIRP-seq signal intensity of Kms27 MM cells transiently transfected with siChe-1A or siControl at co-localizing Che-1/NEAT1 sites ($N = 14{,}654$ sites). Signal intensity from 1 (weak) to 14 (strongest).

Source data are available online for this figure.

performing specific DRIP-qPCR of genes with a high frequency of R-loops (Sanz *et al*, 2016). Indeed, Che-1 depletion induced a strong increase of RNA:DNA hybrids on these regions (Appendix Fig S4C). Of note, NEAT1 depletion also induced an accumulation of R-loops in Kms27 and Kms18 MM cells (Appendix Fig. S4D and E). Finally, RNA:DNA immunoprecipitation and high-throughput sequencing (DRIP-seq) demonstrated that Che-1 depletion causes an accumulation of cellular R-loops on the Che-1/NEAT1 co-binding sites (Figs 4G and EV3E).

Several studies have shown that R-loop formation is prevented by specific RNA-binding proteins involved in RNA biogenesis. These proteins impede R-loop formation by binding to nascent RNA and preventing it from binding to complementary DNA strand. Therefore, their absence favors the genesis of R-loop, the entangled of the transcriptional apparatus on chromatin, and transcription–replication conflicts (Santos-Pereira & Aguilera, 2015; Chakraborty *et al*, 2018; Petti *et al*, 2019). The study by Wu *et al* (2021) showed that most of the proteins enriched by S9.6 are nucleolar RBPs, often involved in ribosomal RNA (rRNA) production or processing, justifying a significant fraction of R-loops at the nucleolus. Che-1, in addition to interacting with RNA Pol II, is predominantly located in the nucleolus and is required for the transcription and maturation of rRNA by interacting with RNA Pol I (Ferraris *et al*, 2012; Bammert *et al*, 2016; Pineiro *et al*, 2018; Kaiser *et al*, 2019; Sorino *et al*, 2020). According to these observations, ChIP-seq analysis showed that Che-1 accumulates on ribosomal DNA and its depletion produced a corresponding accumulation of R-loops on these regions (Fig. 5A and B). To confirm that Che-1 inhibition allows R-loops formation during rRNA transcription, Che-1-depleted Kms27 MM cells were treated or not with Pidnarulex (CX5461), a specific RNA Pol I inhibitor. As shown in Fig. 5C–F, the inhibition of Che-1 led together with an increase in R-loops also a reduction in rRNA transcription, whereas in CX5461-treated cells the inhibition of RNA Pol I coincided with the disappearance of the R-loops, indicating an active role of Che-1 in their prevention linked to transcription. These results were confirmed by treating Che-1 depleted or not Kms27 MM cells with 5,6-dichloro-1-β-D-ribofuranosylbenzimidazole (DRB), a reversibly inhibitor of RNA Pol II elongation. After 2 h of DRB treatment, both siChe-1A and siControl cells showed a complete disappearance of R-loops in the nucleolus, also confirming the observed active role of RNA Pol II in rRNA transcription (Abraham *et al*, 2020). Strikingly, 3 h after drug removal, it was already possible to observe the

Figure 4. Che-1 and NEAT1 suppress RNA:DNA hybrids accumulation.

A Venn diagrams showing the relationship between enriched protein in Che-1 and RNA:DNA hybrids interactome respectively obtained from this study and either Cristini *et al* (2018) (*Left*) and Wu *et al* (2021) (*Right*).

B Chromatin extracts from Kms27 and RPMI8226 MM cells treated or not with RNase H, were subjected to immunoprecipitation with S9.6 antibody and analyzed by WB with the indicated abs. Input corresponds to 5% of the total extract used for immunoprecipitation.

C Representative confocal images showing the interaction between Che-1 and S9.6 revealed by PLA in Kms27 MM cells. Negative controls were performed by omitting Che-1 or S9.6 primary antibody. Scale bar 10 μm.

D Chromatin extracts from Kms27 MM cells transfected with LNA GapmeR NEAT1A or GapmeR Control oligonucleotides were immunoprecipitated with S9.6 antibody and analyzed by WB with the indicated antibodies. Input corresponds to 5% of the total extract used for immunoprecipitation.

E (*Left*) Representative confocal images of Kms27 MM cells treated or not with RNase H, transiently transfected with siChe-1A or siControl and immunostained with S9.6 antibody and. Scale bar 10 μm. (*Right*) Box plot showing S9.6 signal nuclear intensity per cell (Arbitrary Unit-AU). siChe-1A cells are described in green color, while siControl in gray color. One hundred cells were counted in each replicate. Each dot represents a cell. Median scores per sample are written at the top of the median red line. *P* value: $<1.02^{-18}$. ANOVA test was performed to evaluate statistical significance. The red center line denotes the median value (50th percentile) while the black box contains the 25th to 75th percentiles of data. The whiskers mark the 5th and 95th percentiles.

F (*Top*) S9.6 antibody was used for dot blot analysis to evaluate RNA:DNA hybrids formation in Kms27 MM cells by serial dilutions of genomic DNA starting at 1.5 micrograms. *(Bottom)* Quantification of S9.6 levels by densitometric analysis. Values were normalized to a Methylene blue loading control. Error bars represent the standard error of three different biological experiments (Two Tailed *t*-test ***$P < 0.005$, ****$P < 0.001$).

G Enrichment density of DRIP-seq signals at NEAT1/Che1 co-localizing sites in Kms27 MM cells identified in siRNA control (siControl) (gray) and siRNA Che-1 (siChe-1A) (dark green) samples. Enrichment density was calculated on the relative size of each peak (start to end of each fragment) extended 2,000 bp upstream and downstream. Right frame represents the signal obtained from 14,654 randomly selected sites from the same experiments.

Source data are available online for this figure.

© 2022 The Authors

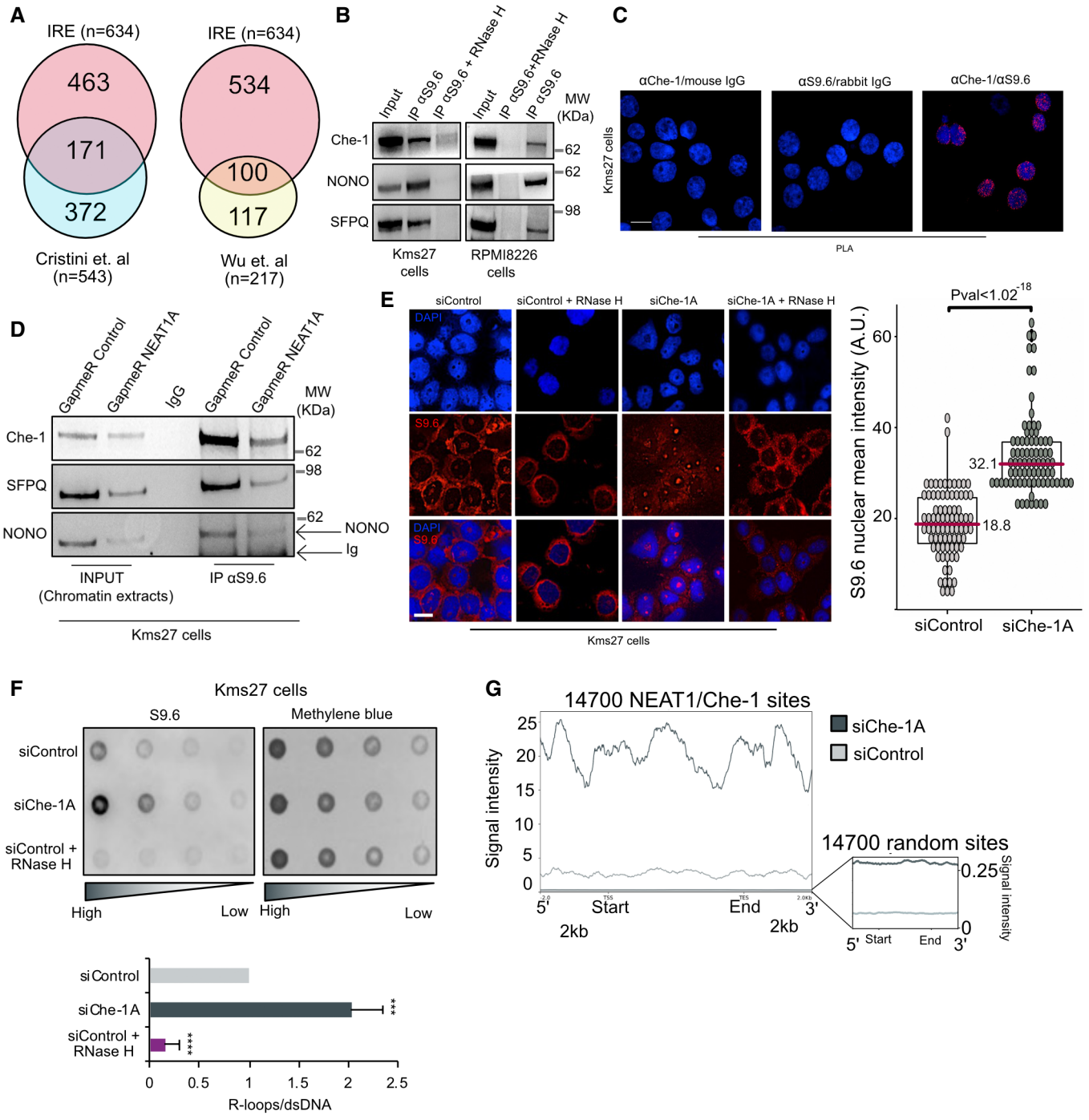

Figure 4.

presence of R-loops in Che-1-depleted cells but not in the control cells (Appendix Fig S5A).

Che-1 controls IFN activation in MM cells

The results shown above demonstrate how Che-1 interacts with NEAT1 on DNA and contributes to prevent RNA:DNA hybrids formation. Che-1 depletion is indeed sufficient to induce increase of RNA:DNA hybrids. Consistent with these findings, RNA sequencing experiments (RNA-seq) in Kms27 MM cells revealed a strong upregulation of many genes involved in NF-kB and both interferon (IFN) type I (IFN alpha and beta) and type II (IFN gamma) signaling in Che-1-depleted cells (Fig. 6A–C), in line with what observed in several cell models where antiviral response is a fundamental mechanism in response to DNA damage (Lim *et al*, 2015; Shen *et al*, 2015). Indeed, Che-1-depleted cells exhibited a strong activation of the RNA:DNA sensor pathway cGAS-Sting (Motwani *et al*, 2019; Hopfner & Hornung, 2020) and the RNA helicase RIG-I,

 © 2022 The Authors

involved in double-stranded RNA-induced innate antiviral response (Yoneyama *et al*, 2004; Fig 6D; Appendix Fig S6A). Notably, similar results were obtained from an RNA-seq analysis of Kms27 MM cells with or without NEAT1 depletion (Appendix Fig. S6B–D), underscoring a common functional role played by Che-1 and NEAT1. We validated these results by taking advantage of a NF-kB-luciferase reporter assay. As shown in Fig 6E, Che-1 depletion was able to activate luciferase activity at the same levels observed by the overexpression of RelA/p65 protein, the principal member of the NF-kB complex (Nolan *et al*, 1991). Of note, both IFNB (Interferon beta) and IFNG (Interferon gamma) were upregulated in Che-1-depleted cells (Fig. 6F and G; Appendix Fig. S6E and F), and the increase of transcript abundance of NF-kB and IFN target genes confirmed the activation of these pathways (Fig 6G). Notably, Che-1

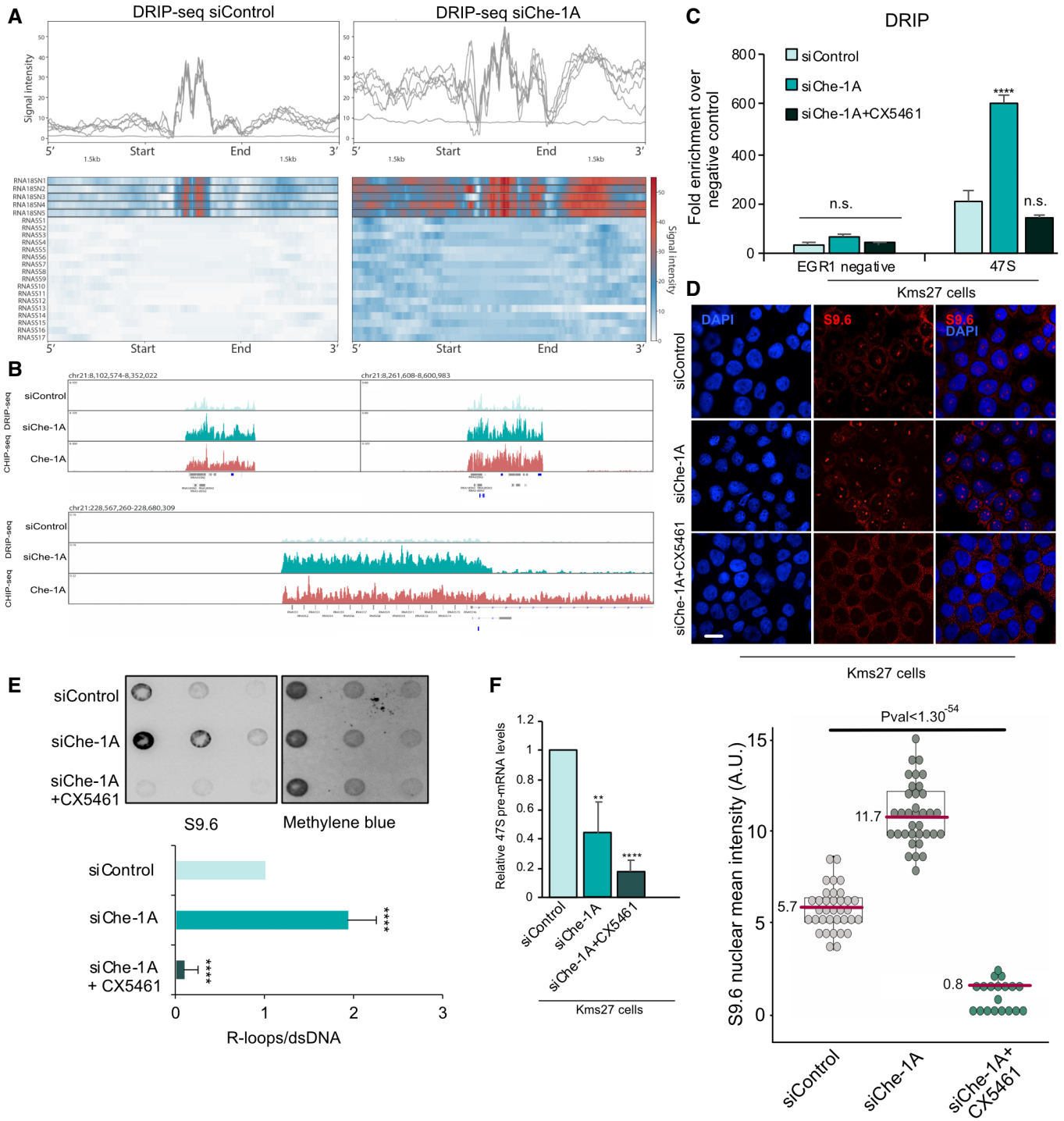

Figure 5.

© 2022 The Authors

Figure 5. Che-1 and NEAT1 prevent RNA:DNA hybrids formation during transcription.

A Signal intensity plot (Top) of DRIP-seq enrichment in control KMS27 cell (left) and upon the siChe-1A interference (*right*) at ribosomal gene loci. Each line represents a single genomic locus. The genomic window was extended 1.5 kb upstream and downstream of each ribosomal gene locus. Normalized DRIP-seq signals at all the selected ribosomal genes were then plotted in a heatmap (Bottom) using the following color scheme: Red: high enrichment, Blue: lower enrichment.

B Screenshots of DRIP-seq (light and dark green color) and ChIP-seq (red color) enrichment at selected ribosomal genes loci. The coordinates of each genomic window are depicted above each frame (HG38).

C DRIP-qPCR enrichment of the indicated genes in Kms27 cells transiently transfected with siChe-1A or siControl and treated or not with CX5461. Data are expressed as percent of Input. Error bars represent the standard error of three different biological experiments performed in technical duplicate (Two Tailed *t*-test ****$P < 0.001$, n.s. = not significant).

D *(Top)* Representative confocal images of Kms27 MM cells transfected and treated as in C and immunostained with S9.6 antibody. Scale bar 10 μm. *(Bottom)* Box plot showing S9.6 signal nuclear intensity per cell (Arbitrary Unit-AU). siChe-1A cells are described in dark gray, siChe1A plus CX5461 in green color, while siControl in gray color. Median scores per sample are written at the top of the median red line. *P* value: $<1.30^{-54}$. ANOVA test was performed to evaluate statistical significance. The red center line denotes the median value (50th percentile) while the black box contains the 25th to 75th percentiles of data. The whiskers mark the 5th and 95th percentiles.

E *(Top)* Dot blot analysis of decreasing amounts of genomic DNA extracts from Kms27 MM cells depleted or not for Che-1 expression (siChe-1A) and treated with CX5461, were probed using abs directed against RNA:DNA hybrids. *(Bottom)* Quantification of S9.6 levels by densitometric analysis. Values were normalized to a Methylene blue loading control. Error bars represent the standard error of three different biological experiments (Two Tailed *t*-test ****$P < 0.001$).

F RT-qPCR analysis of 47S pre-rRNA levels of Kms27 MM cells transiently transfected with siChe-1A or siControl and treated or not with CX5461. Values were normalized to Actin expression. Error bars represent the standard error of three different biological experiments performed in technical duplicate (Two Tailed *t*-test **$P < 0.01$, ****$P < 0.001$).

overexpression completely rescued these effects (Appendix Fig. S6G and H). In agreement, we found similar results in NEAT1-depleted Kms27 and Kms18 MM cells (Appendix Fig. S6I–K). Strikingly, IFN activation and DNA damage induced by Che-1 depletion was completely reversed by overexpressing GFP-RNase H (Fig. 6H and I). Overall, these results demonstrate that Che-1 and NEAT1 prevent IFN response in MM cells by facilitating RNA:DNA hybrids resolution.

MM patients exhibit high levels of RNA:DNA hybrids and IFN activation

These analyses support a pivotal role of the Che-1/NEAT1 interaction in conferring a survival advantage to cells during stress. We first translated these findings by leverage ~1,100 MM patient transcriptomes from the CoMMpass data set and Oncomine database (Agnelli *et al*, 2009), then we evaluated RNA:DNA hybrids levels in a MM patient's cohort. Previous studies have demonstrated a consistent association between the expression of Che-1 and NEAT1 and the progression of MM (Desantis *et al*, 2015; Taiana *et al*, 2019, 2020; Bruno *et al*, 2020). The analysis of Oncomine database (Agnelli *et al*, 2009) confirmed these observations (Fig EV4A). This prompted us to investigate whether same results would have been obtained from querying the International Staging System (ISS) available in the CoMMpass dataset. Notably, this analysis showed that not only the expression of Che-1, but also of NEAT1 and numerous components of the paraspeckle, were significantly higher in ISS stage 3 compared to ISS 1 and ISS 2 (Fig EV4B). In addition, survival analysis of 542 MM (Hanamura *et al*, 2006) showed that high expression of Che-1 and NEAT1 are strongly associated with poorer prognosis in MM (Appendix Fig S7A). Moreover, we downloaded and split this cohort into the two different treatment strategies (TT2 and TT3) and we measured the prognostic value of NEAT1, NONO, and SFPQ in the 2 treatment strategies separately, observing that

Figure 6. Che-1 controls Interferon activation in MM cells.

A Differential analysis of siControl vs. siChe1A transcriptome in Kms27 MM cells. Volcano plot shows 135 significantly upregulated (dark green) and 392 downregulated genes (dark gray). *x*-axis reports the base-2 logarithm of fold change which is approximated to the *B* value coming from the statistical Wald test. *y*-axis reports the base-10 logarithm of *Q* value of significant genes.

B Heatmap depicting pathway activity scores for each transcriptome sample according to PROGENy. The activity score is shown as shade ranging from blue to red which indicates the level of pathway activation. Blu = nonactive; Red = active.

C Gene Set Enrichment Analysis (GSEA) of upregulated significant differential genes with their relative base-10 logarithm of *Q* value. The analysis was based on hallmark gene sets collection.

D WB analysis of total extracts of Kms27 MM cells depleted or not for Che-1 (siChe-1A) and probed for the indicated abs.

E *(Left)* Luciferase activity of human NF-kB promoter was measured in Kms27 MM cells transiently transfected with siChe-1A or siControl oligonucleotides or with empty vector or p65/RelA protein expressing vector. Error bars represent the standard error of three different biological experiments performed in duplicate (Two Tailed *t*-test ***$P < 0.005$, ****$P < 0.001$). *(Right)* WB analysis of total extracts of Kms27 MM cells transiently transfected as described in E and incubated with the indicated antibodies.

F, G RT-qPCR analysis of the levels of the indicated genes in Kms27 MM cells transiently transfected with siChe-1A or siControl. Values were normalized to Actin expression. Error bars represent the standard error of three different experiments in duplicate (Two Tailed *t*-test ***$P < 0.001$, ****$P < 0.001$).

H WB analysis for the indicated antibodies of total extracts from Kms27 MM cells with siChe-1A or siControl and where indicated with GFP-tagged RNaseH expression vectors.

I RT-qPCR analysis of IFNB and IFNG levels in Kms27 MM cells transiently transfected as in H. Values were normalized to Actin expression. Error bars represent the standard error of three different biological experiments performed in duplicate (Two Tailed *t*-test **$P < 0.01$, ***$P < 0.005$.)

Source data are available online for this figure.

© 2022 The Authors

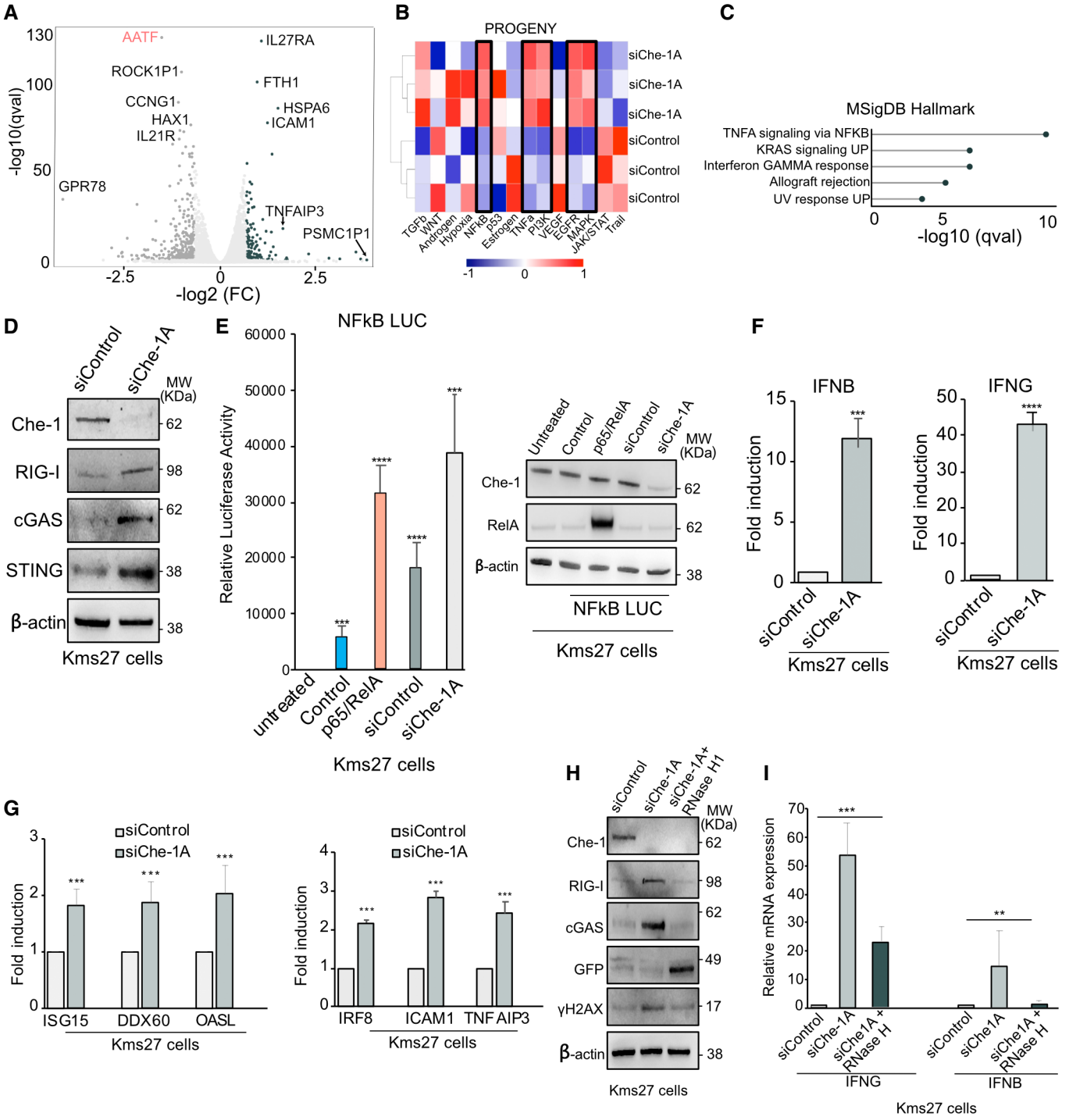

Figure 6.

prognostic value does not change in TT2 and TT3 cohorts (Appendix Fig S7). We also observed that interrogating the CoMMpass cohort resulted in assigning to NONO, SFPQ, and Che-1 a significant prognostic value. Conversely, NEAT1 failed in having significant prognostic power associated with its relative expression, probably due to the bulk RNA-seq analysis, where identifying the abundance of both isoforms separately remains challenging (Appendix Fig S7C). We also explored the link between the expression of NONO, SFPQ, NEAT1, and Che-1 genes in relationship with the main genetic events in multiple myeloma together with controls, such as International Staging System (ISS), and therapy using multivariate analysis. The results confirmed a solid prognostic role of SFPQ together with the Che-1 gene. NONO bordered on the level of significance of P-value = 0.05 while NEAT1 was not prognostic

© 2022 The Authors

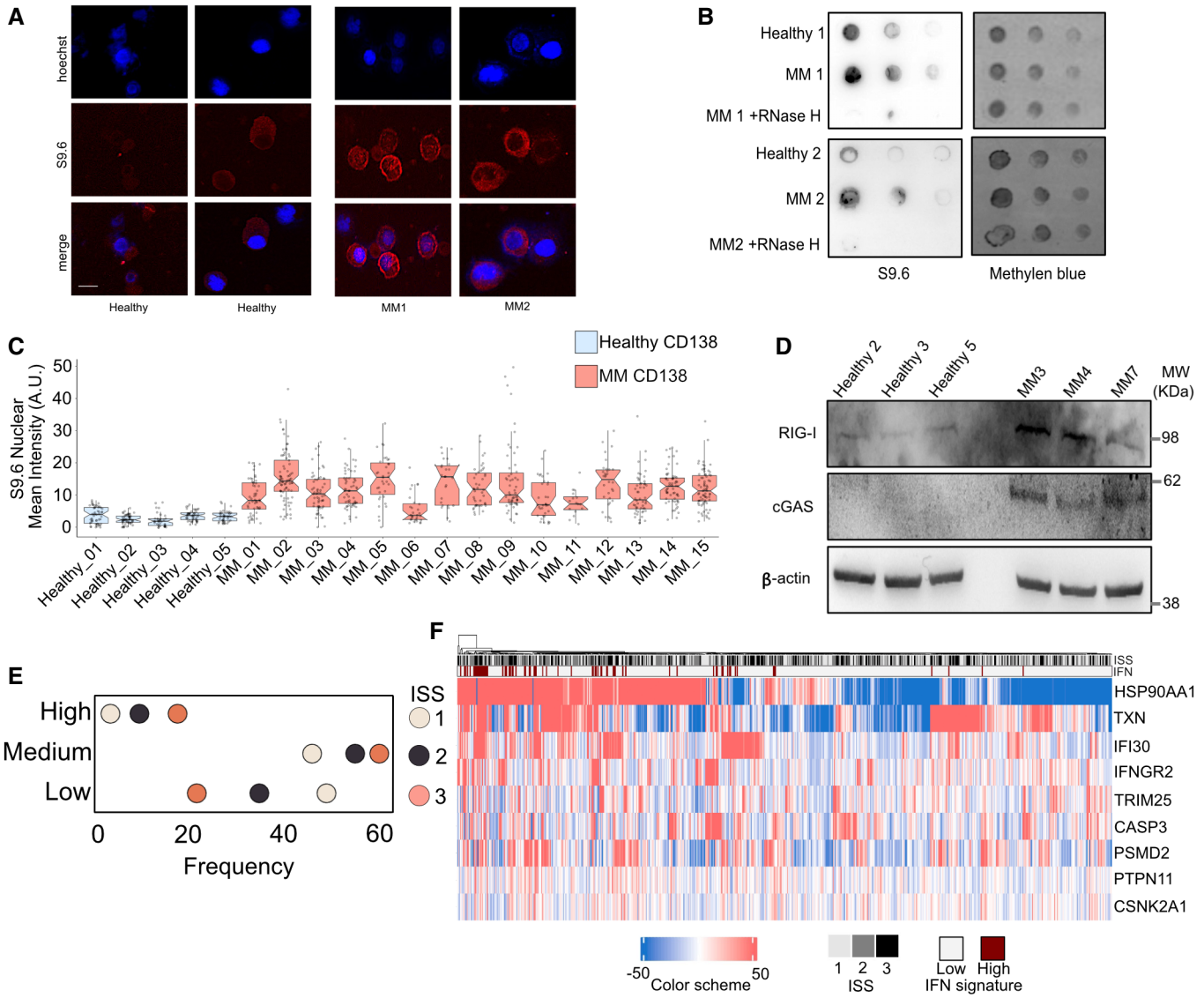

Figure 7. MM patients exhibit high levels of RNA:DNA hybrids and IFN activation.

A Representative S9.6 immunofluorescence levels in healthy and tumor CD138$^+$ plasma cells purified from patient bone marrow. Nuclei were visualized by staining with Hoechst dye. Scale bar 10 μm.

B Dot blot performed to evaluate the enrichment of RNA:DNA hybrids formation using the S9.6 antibody by serial dilutions of genomic DNA starting at 1.0 μg. Methylene blue normalization of S9.6 signal image acquired by using Alliance Mini HD6 system by UVITEC Ltd.

C Boxplot showing relative S9.6 nuclear mean intensity in CD138$^+$ plasma cells from 15 MM patients (red) and 5 healthy (light blue). Dot plot representing each cell considered overlay the boxplot. *Y*-axis: S9.6 Nuclear Mean Intensity (AU). The center line denotes the median value (50th percentile) while the boxes contain the 25th to 75th percentiles of data. The whiskers mark the 5th and 95th percentiles.

D Representative WB analysis with the indicated antibodies of healthy and neoplastic CD138$^+$ purified plasma cells from patients.

E Proportion of CoMMpass patients (N = 687) assigned to the IFN signature category in relationship with the relative ISS stage. Each patient was assigned to the IFN signature category: High (*Top*), Medium (*Middle*) Low (*Bottom*). Dot colors correspond to the ISS stage of samples for each IFN signature category.

F Unsupervised clustering heatmap showing enrichment profiles of 9 IFN signature genes. From the top: ISS stages 1,2,3 of each patient (N = 687). IFN signature High (red, N = 71) and Low (white, N = 614) assigned to each patient. Color scheme representing up- (red) and down- (blue) regulation of the selected genes across the patient dataset. Colors are proportional to normalized (cpm) read enrichment – the relative read enrichment median of each gene within the full patient cohort.

Source data are available online for this figure.

(Table EV2 and Appendix Table S1). Then, we assessed RNA:DNA hybrids levels in MM patients. Remarkably, immunofluorescence analysis of 15 samples of CD138$^+$ MM cells and five samples from healthy controls showed a significant higher level of hybrids in most MM patients (Fig. 7A–C), and both cGAS and RIG-I levels strongly increased in MM cells compared with normal plasma cells (Fig 7D).

© 2022 The Authors

Accordingly, transcriptomic analysis if CoMMpass dataset revealed a close association between ISS grade and activation of IFN pathway (Fig. 7E and F). Moreover, a high expression of this pathway was associated with poorer prognosis in the patient cohort selected by IFN gene signature expression (Fig EV4C; Table EV3 and Appendix Table S1) and in the selection of patients exhibiting the highest expression of the signature (Fig EV4D). Then, we evaluated the correlation between the expression of Che-1 and the IFN gene signature. Although the large amount of expression heterogeneity of MM tissues and the numerous biases impacting this kind of analysis from real patient data, we found a positive Pearson correlation of 0.16 (Appendix Fig S7D). Moreover, the analysis of association of

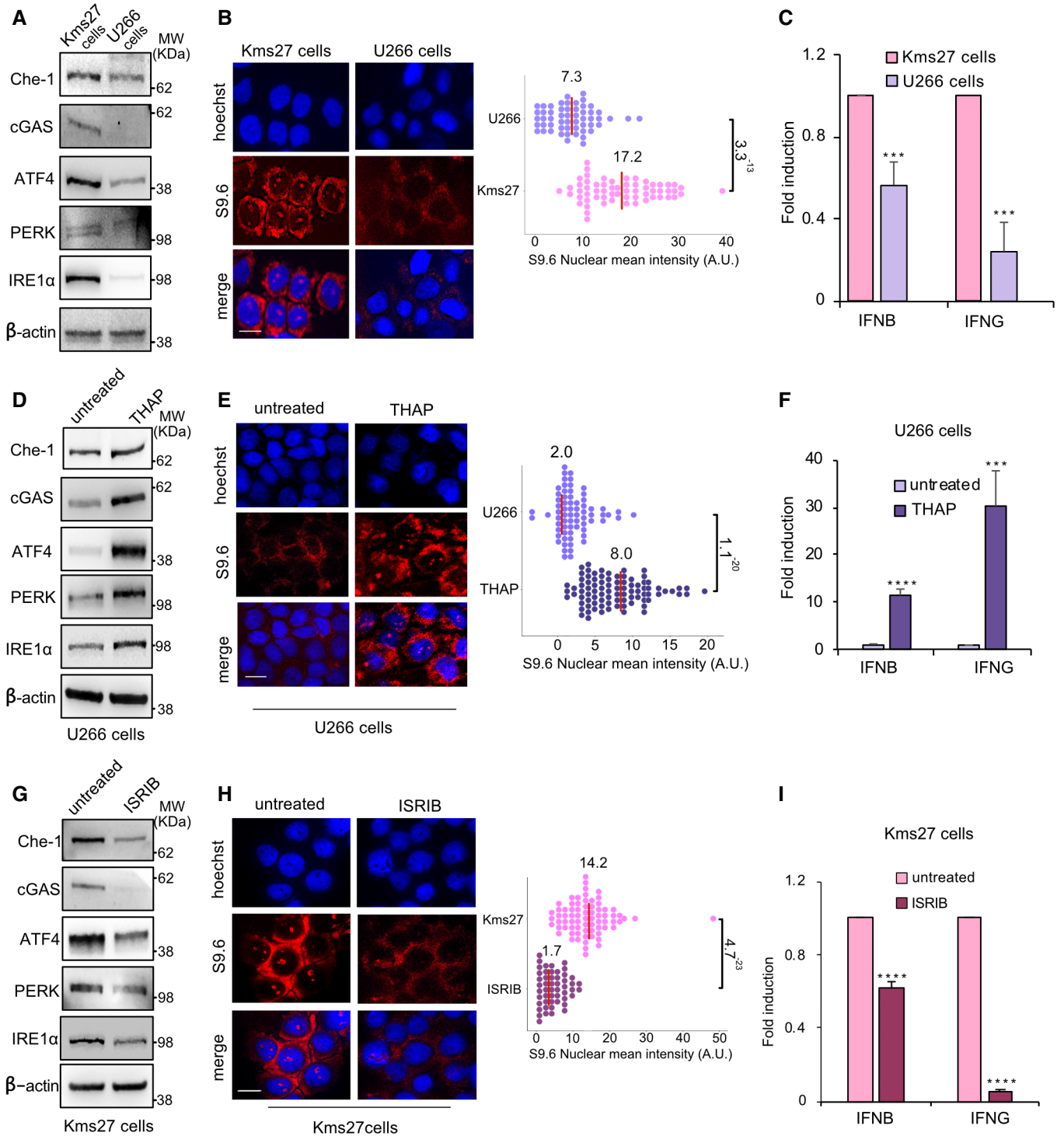

Figure 8.

Figure 8. UPR induced R-loops in MM cells.

A WB analysis of total extracts from Kms27 and U266 human MM cells with the indicated abs.

B (*Left*) Kms27 and U266 MM cells were subjected to immunostaining with S9.6 antibody Scale bar 10 μm. (*Right*) Dot plot showing relative S9.6 nuclear mean intensity cell in the nucleus. One hundred cells were counted in each replicate. Median scores per sample are written at the top of the median red line. *P* value: 3.3^{-13}. *T*-test was performed to evaluate statistical significance.

C Different expression of IFNG and IFNB in Kms27 and U266 MM cells was assessed by RT-qPCR. Values were normalized to Actin expression. Error bars represent the standard error of three different biological experiments performed in duplicate (Two Tailed *t*-test ***$P < 0.005$).

D WB analysis with the indicated abs of total extracts from U266 MM cells treated or not with Thapsigargin (THAP) 0.5 μg/ml for 16 h.

E (*Left*) U266 MM cells treated or not with THAP as in (D) and immunostained with S9.6 antibody Scale bar 10 μm. (*Right*) Dot plot showing relative S9.6 nuclear mean intensity per cell. One hundred cells were counted in each replicate. Median scores per sample are written at the top of the median red line. *P* value: 1.1^{-20}. *t*-test was performed to evaluate statistical significance.

F RT-qPCR analysis of IFNG and IFNB in U266 MM cells treated or not with THAP. Values were normalized to Actin expression. Error bars represent the standard error of three different biological experiments performed in duplicate (Two Tailed *t*-test ***$P < 0.005$, ****$P < 0.001$).

G WB with indicated abs of total extracts from Kms27 MM cells treated or not with ISRIB 1 μM for 6 h.

H (*Left*) Immunostaining with S9.6 antibody of Kms27 MM cells treated or not with ISRIB as in (G) Scale bar 10 μm. (*Right*) Dot plot showing relative S9.6 nuclear mean intensity per cell. One hundred cells were counted in each replicate Median scores per sample are written at the top of the median red line. *P* value: 4.7^{-23}. *t*-test was performed to evaluate statistical significance.

I RT-qPCR analysis of IFNG and IFNB levels in Kms27 MM cells treated as in (G). Values were normalized to Actin expression. Error bars represent the standard error of three different biological experiments performed in duplicate (Two Tailed *t*-test ****$P < 0.001$).

Source data are available online for this figure.

IFN gene signature and Che-1 expression in a multivariate analysis in the same cohort identified a strong significant prognostic link between the 2 variables together with the ISS scoring (Table EV4). Finally, utilizing the CoMMpass IFN signature, we performed a differential analysis between the transcriptome of the patients classified as IFN HIGH and IFN LOW to measure the differential pathways and gene players linked with the IFN HIGH phenotype. We observed a direct link between the upregulation of genes in IFN HIGH associated with G2M checkpoint (DNA damage) and activation of E2F target genes (a marker of proliferation) in GSEA analysis (Appendix Fig S7E). Then, we measured together in a multivariate analysis the prognostic association of the IFN HIGH and IFN LOW patient selection with several genes involved in transcription/replication conflicts and upregulated in MM (Dutrieux *et al*, 2021). This approach showed that the identification of the IFN signature systematically recapitulates previous findings (Table EV5). Taken together, these results indicate a strong association between elevated levels of RNA:DNA hybrids, the expression of paraspeckle genes, and the activation of the IFN response.

UPR induced R-loops in MM cells

We then sought to identify the mechanism underlying the elevated levels of RNA:DNA hybrids that we found in MM cells. Recently, it has been demonstrated that the Integrated Stress Response (ISR) induces R-loops in U2OS cells (Choo *et al*, 2020). Since a peculiar characteristic of MM cells is a high Unfolded Protein Response (UPR) due to their abnormal production of immunoglobulins (Nikesitch *et al*, 2018), it is conceivable that this type of stress may contribute to the generation of R-loops. To test this hypothesis, we took advantage of two different MM cell lines endowed with different levels of UPR (Kms27 high UPR, U266 low UPR). As shown in Fig. 8A–C and Appendix Fig. S8A and B, elevated UPR activation in Kms27 MM cells was found strongly associated with higher levels of R-loops and IFN expression when compared to U266 MM cells. In agreement, both Che-1 and NEAT1 also resulted more expressed in Kms27 than U266 MM cells (Fig. 8A; Appendix Fig S8A). To further investigate this association, we induced UPR in U266 MM cells using thapsigargin (THAP). Increased expression of ATF4, PERK, and IRE1α confirmed UPR activation, together with an augment of Che-1 and NEAT1 levels (Fig. 8D; Appendix Fig S8C). Strikingly, treatment with THAP produced a dramatic increase of both RNA:DNA hybrids and IFN expression (Fig. 8E and F; Appendix Fig S8D). To confirm these findings, we treated Kms27 MM cells with ISRIB, a selective inhibitor of Integrated Stress Response (ISR) that impairs adaptation to ER stress (Sidrauski *et al*, 2013; Tsai *et al*, 2018; Zyryanova *et al*, 2018). As shown in Fig 8G, Kms27 MM cells treated with this drug exhibited a strong reduction of UPR activation, and both Che-1 and NEAT1 expression, associated with decreased levels of R-loops and IFN activity (Fig. 8G–I; Appendix Fig. S8E and F).

These results were further confirmed by treating with ISRIB two primary human MM cell lines (MM196 and MM 217; Bruno *et al*, 2020; Fig EV5A–D).

Overall, these results demonstrate that UPR induces R-loops and inflammatory signaling in MM cells.

Discussion

In this study, we demonstrate that Che-1 is a component of paraspeckles. Che-1 physically interacts with the NEAT1 lncRNA in MM cells and provide evidence that these two molecules widely colocalize on DNA sites. We show that Che-1 and NEAT1 bind R-loops and are required for their resolution, preventing their accumulation and inflammatory response activation. We also show that high levels of RNA:DNA hybrids are present in MM patients and that activation of IFN response correlates with the stage of the disease and is a negative prognostic factor. Finally, we provide evidence that unfolded protein response (UPR) in MM cells promotes the formation of R-loops and the consequent activation of IFN response.

Paraspeckles are subnuclear bodies of which the NEAT1 lncRNA is the main structural component, necessary for their formation and maintenance (Fox & Lamond, 2010). Although numerous studies over the last few years have outlined a role of these structures in

 © 2022 The Authors

RNA and protein retention, NEAT1 has also been found to localize to transcriptional start sites of numerous genes, hypothesizing its active role in the regulation of gene transcription (West *et al*, 2014). Our results confirm the presence of NEAT1 on DNA in over 25,000 sites (Fig 2C), with an accumulation on the coding regions, reinforcing the finding that NEAT1 plays an important role in transcription. Moreover, our results demonstrate that NEAT1 and Che-1 colocalize onto the DNA, and that NEAT1 is required for recruiting Che-1 on these sites. Therefore, it is conceivable a scenario in which NEAT1 can act as a hub to concentrate paraspeckles components involved in the transcription or maturation of RNA on specific DNA sites. Our results also demonstrated that Che-1 and NEAT1 interact with the RNA:DNA hybrids present on DNA, and that the presence of NEAT1 is required to recruit not only Che-1, but also other paraspeckle components such as NONO or SFPQ onto these structures, reinforcing the hypothesis that NEAT1 performs an important hub function. Of note, NEAT1, and especially Che-1, appear necessary for the control of R-loops formation, given the massive accumulation of these structures on the binding sites of Che-1, when the expression of the latter is inhibited. According to these results, immunofluorescence experiments in Che-1-depleted cells showed an extensive accumulation of R-loops in the nucleoli, the main site of active transcription and where Che-1 is mostly found. In agreement with these results, RNA-seq experiments showed how the depletions of Che-1 or NEAT1 produce the activation of NF-kB and IFN pathways through the DNA-sensing receptor cyclic GMP–AMP synthase (cGAS) (Motwani *et al*, 2019; Hopfner & Hornung, 2020), reinforcing the notion that these two molecules are involved in the resolution of RNA:DNA hybrids.

Recently, Che-1 has been shown to regulate chromatin accessibility (Bruno *et al*, 2020). Further studies will define its role in the control of R-loops depends on this function or if these are two distinct functions of the protein.

It has been demonstrated that expression of both NEAT1 and Che-1 increases in response to several types of stress. The higher levels of NEAT1 are deemed necessary for a greater production of paraspeckles to sequester protein and RNA molecules and allow the cell to be able to respond adequately to the insult received. However, since most cellular stresses, as indeed viral infections, lead to an accumulation of RNA:DNA hybrids, it is also possible that Che-1 together with the other molecules of the paraspeckle, plays an active role on these hybrids, thus containing the generation of DNA damage and even cell death.

We further report increased levels of NEAT1 and paraspeckles genes during MM progression, and these data were further confirmed by clinical data available in CoMMpass data set. Moreover, the expression of NEAT1, Che-1, and other paraspeckles genes were found associated with reduced overall survival of MM patients. Remarkably, these findings concur with our finding that MM patients exhibit elevated levels of RNA:DNA hybrids compared to healthy controls, and this phenomenon appears to be related to disease progression, given that activation of IFN pathway is significantly found in ISS 3 and is markedly associated with a poor prognosis and Che-1 expression. In agreement with our results, several proteins involved in Transcription/Replication Conflicts (TRC) and identified in the R-loop interactome are overexpressed associated with a poor outcome in MM patients (Dutrieux *et al*, 2021).

It has recently been shown that cellular stress is capable of producing high levels of RNA:DNA hybrids (Choo *et al*, 2020). Therefore, the presence of a high quantity of these structures in MM patients could be produced by the constitutive UPR that distinguishes this pathology. In support of this hypothesis, our results from UPR modulation in MM cells confirmed a direct correlation between this type of stress, and the levels of RNA:DNA hybrids along with IFN response. Furthermore, it has recently been shown that proteasome inhibition induced by some drugs commonly used in the treatment of MM produces a broad-scale interference with spliceosome function (Huang *et al*, 2020), indicating a possible alternative molecular mechanism for the generation of RNA:DNA hybrids.

Our results show a direct correlation between MM progression and IFN activation. Sterile trigger of inflammation has been described to play an important role in the formation and maintenance of multipotent hematopoietic stem and progenitor cells (HSPCs) (Sawamiphak *et al*, 2014; Pietras, 2017; Espin-Palazon *et al*, 2018). It is very interesting to underline how a very recent study has identified the imbalance of R-loops as the cause of the activation of sterile inflammation in HSPCs, identifying an important link between R-loops, inflammation, and the development of the hematopoietic system (Weinreb *et al*, 2021). In addition, they found a strong correlation between inflammatory signaling and bone marrow blasts (Weinreb *et al*, 2021). It is therefore possible to hypothesize a model in which MM cells might take proliferative advantage from a high UPR, producing RNA:DNA hybrids, and triggering an inflammatory cascade (Fig 8). In this context, the elevated Che-1 and NEAT1 expression levels observed in MM, could help to keep the levels of RNA:DNA hybrids under constant control, preventing extensive genomic damage, and cell death (Fig 8). Of course, further additional experiments are needed to understand the real relevance of these mechanisms in MM, but our results identify a new important role of Che-1 and NEAT1 in this pathology and reinforce the notion that these molecules can be considered important therapeutic targets.

Material and Methods

Reagents and Tools table

Experimental models	Source	Identifier or catalog number
Multiple Myeloma Patient Sample (isolation CD138^{+} from Bone Marrow)	Fanciulli Lab	Hematological Unit of Regina Elena Cancer Institute
MM196 primary Multiple Myeloma (MM) cells	Fanciulli Lab	Hematological Unit of Regina Elena Cancer Institute

© 2022 The Authors

Reagents and Tools table (continued)

Experimental models	Source	Identifier or catalog number
MM217 primary MM cells	Fanciulli Lab	Hematological Unit of Regina Elena Cancer Institute
Kms27 MM cells	Drs. Petrucci	Sapienza University of Rome
Kms18 MM cells	Drs. Petrucci	Sapienza University of Rome
U266 MM cells	Drs. Folgiero	Bambino Gesù Hospital, Rome
RPMI8226 MM cells	Prof. Lunghi	University of Parma
Bacterial strains		
XL1 blue	Stratagene	
Recombinant DNA		
PCS2-MT-AATF (MYC-Che-1)	Fanciulli Lab	For mammalian expression of MYC tagged AATF/Che-1 protein
pEGFP-RNase H1 (plasmid #108699)	Addgene	For mammalian expression of RNase H1 protein
p65/RelA	Karin Lab	For mammalian expression of p65.
NFkB-luc reporter	Karin Lab	Reporter for Luciferase Assay
Antibodies		
Rabbit Polyclonal anti-Che-1 (WB, 1:1,000, IF 1:200; IP and RIP 5 μg)	Millipore	Cat# ABC953
Rabbit Polyclonal anti-Histone H3 (1:1,000)	Abcam	Cat# ab1791
Mouse Monoclonal anti-β-actin (WB 1:10,000)	Sigma Aldrich	Cat# A5441
Rabbit Polyclonal gH2AX (JBW301) (WB 1:1,000)	Millipore	Cat#05-636
Rabbit Polyclonal anti-SFPQ (WB 1:500)	Bethyl	Cat# A301-322A
Rabbit Polyclonal anti-NONO (WB 1:500)	Bethyl	Cat# A300-587A
Mouse Monoclonal anti SFPQ (IF 1:500; IP 5 μg)	ThermoFisher	Cat# MA1-25325
Mouse Monoclonal anti-NONO (78-1 C) (IF 1:500; IP 5 μg)	ThermoFisher	Cat# MA3-2024
Rabbit Polyclonal anti-cGAS (E5V3W) (WB 1:1,000)	Cell Signaling	Cat# 79978
Rabbit Polyclonal anti-RIG-I (D33H10) (WB 1:1,000)	Cell Signaling	Cat# 4200
Rabbit Polyclonal anti-ATF4 (D4B8) (WB 1:1000)	Cell Signaling	Cat# 11815
Rabbit Polyclonal anti-PDI (C81H6) (WB 1:1000)	Cell Signaling	Cat# 3501
Rabbit Polyclonal anti-PERK (D11A8) (WB 1:1,000)	Cell Signaling	Cat# 5683
Rabbit Polyclonal anti-IRE1α (14C10) (WB 1:1,000)	Cell Signaling	Cat# 3294
Rabbit Polyclonal anti-GFP (D5.1) (WB 1:500)	Cell Signaling	Cat# 2956
Mouse Monoclonal anti-S9.6 (DRIP and RIP 3μg; DOT BLOT 1:1,000; IF 1:500)	Kerafast	Cat# ENH001
Rabbit Polyclonal anti-STING (D2P2F) (WB 1:1,000)	Cell Signaling	Cat# 13647
Mouse anti-αTubulin (DM1A) (WB 1:500)	Calbiochem	Cat# CP06
Rabbit Polyclonal anti-Fibrillarin (IF 1:100)	Abcam	Cat# ab5821
Alexa Fluor 594-anti-Rabbit (IF 1:500)	ThermoFisher	Cat# A11037
Alexa Fluor 594-anti-Mouse (IF 1:500)	ThermoFisher	Cat# A11032
Alexa Fluor 488-anti-Rabbit (IF 1:500)	ThermoFisher	Cat# A11034
Alexa Fluor 488-anti-Mouse (IF 1:500)	ThermoFisher	Cat# A11001
Goat anti-Rabbit-HRP (WB 1:10,000)	Biorad	Cat# 170-6515
Goat anti-Mouse-HRP (WB 1:5,000)	Biorad	Cat# 170-6516
Oligonucleotides and other sequence-based reagents		
PCR Primers	This study	Table EV1
Chemicals, Enzymes and other reagents		
Pidnarulex (CX5461)	SelleckChem	Cat # S2684

© 2022 The Authors

Reagents and Tools table (continued)

Experimental models	Source	Identifier or catalog number
5,6-Dichlorobenzimidazole 1-β-D-ribofuranoside (DRB)	Sigma Aldrich	Cat#1916
ISRIB	Sigma Aldrich	Cat# SML0843
Thapsigargin	Sigma Aldrich	Cat# T9033
DMSO	Santacruz	Cat# sc-358801
RNase T1	ThermoFisher	Cat# EN0541
Shortcut RNase III	New England Biolabs	Cat# M0245S
RNase H1	New England Biolabs	Cat# M297S
Software		
ImageJ		
Zeiss Zen	Zeiss (GERMANY)	
FASTQC v0.11.9	http://www.bioinformatics.babraham.ac.uk/projects/fastqc/	
MultiQC v.1.9	Ewels *et al* (2016)	
bowtie2 v.2.3.5.1	Langmead & Salzberg (2012)	
SAMtools v.1.2	Li *et al* (2009)	
GATK4 suite v.4.1.8.1		
MACS2 v.2.2.6		
bedGraphToBigWig v.4	Kent *et al* (2010)	
HOMER v.4.11	Heinz *et al* (2010)	
DeepTools v.3.5.0		
bedtools v2.29.2		
LIMMA v3.44.3	Ramirez *et al* (2014)	
Kallisto v.0.46.0	Bray *et al* (2016)	
Sleuth v.0.30.0	Pimentel *et al* (2017)	
MultiQC v.1.92		
PROGENy v.1.10.0	Schubert *et al* (2018)	
edgeR v3.13	Robinson *et al* (2010)	
Survfit v.3.1.12		
survminer v.0.4.819		
Other		
Qubit 2.0 fluorometer	Life Technologies	
NextSeq 500	Illumina	

For Antibodies: DRIP, DNA/RNA Immunoprecipitation; IF, Application Immunofluorescence; IP, Immunoprecipitation; RIP, RNA Immunoprecipitation; WB, Western Blot.

Methods and Protocols

Cell lines and cell culture treatment

Human multiple myeloma cell lines Kms27, Kms18, U266, RPMI-8226, and two primary MM cell line MM196 and MM217 (Bruno *et al*, 2020) were cultured in Optimem (Thermo Fisher Scientific) supplemented with 15% inactivated Fetal Bovine Serum (FBS) (Thermo Fisher Scientific), 2 mM of glutamine and 40 μg/ml of gentamicin. All cell lines were cultured at 37°C, in a humidified atmosphere with 5% CO_2 and mycoplasma contamination was periodically checked by polymerase chain reaction (PCR) analysis. All the cell lines were not listed in the ICLAC database of commonly misidentified cell lines and were authenticated at The San Martino Hospital Genomics Facility using short tandem repeat DNA profiling. The presence of the Epstein–Barr virus (EBV) was detected by PCR analysis.

Transfection with siRNA and DNA constructs

All the transfection experiments were carried out using the Lipofectamine 3000 reagents according to the manufacturer's instructions (Thermo Fisher Scientific). Cells were analyzed 48 h after transfection, and the efficiency of transfection was determined by RT-qPCR, immunoblotting, or immunofluorescence. Stealth siRNA oligonucleotides targeting Che-1 (siChe-1A, cat. n. 1299003–HSS120158 and siChe-1B, cat. n. 1299003–HSS120159) or a control sequence (siControl, cat. n. 12935300) were purchased from Thermo Fisher

© 2022 The Authors

Scientific. pEGF-RNaseH1 expression vector was purchased from Addgene (plasmid #108699). RelA expressing vector and NF-kB-luc reporter were a gift Dr. Karin from University of San Diego, La Jolla (CA). LNA oligonucleotides were provided by Exiqon (Vedbaek, Denmark). Custom Long Non-Coding LNA GapmeRs (NEAT1A, NEAT1B and Control) were custom-designed and purified by HPLC followed by Na^+−salt exchange and lyophilization. LNA GapmeRs were used at 100 nM.

Human specimens

MM patient samples were collected as part of routine clinical examination. The study was approved by the Regina Elena Cancer Institute Ethics Committee (CE 422/14) and written informed consent to participate in this study was provided by all subjects. Bone marrow aspirates from healthy donor and pathological patients were enriched for plasma cells by magnetic cell separation using a human CD138 positive selection and Macs Separator kits (Miltenyi Biotec, Germany).

Western blot and coimmunoprecipitation

Immunoblotting and coimmunoprecipitation were performed as previously described (Bruno *et al*, 2010). Detailed information for all antibodies is provided in Reagents and Tools Table.

Luciferase assay

Cell extracts were prepared and assayed for luciferase activity according to the manufacturer's instructions (Promega, WI) using the GloMax Luminometer (Promega, WI). Total protein quantification in the extracts was determined by Bradford assay, and luciferase activity of equal amounts of proteins was determined.

RNA isolation and quantitative real-time PCR

Total RNA was extracted from the same number of viable cells using QIAzol Lysis Reagent (Qiagen). cDNA was synthesized from equal amount of RNA by reverse transcription using M-MLV reverse transcriptase (Thermo Fisher Scientific) and a mixture of random primers (Thermo Fisher Scientific). This single-stranded cDNA was then used to perform quantitative real-time PCR (RT-qPCR) with specific primers using a PowerUp SYBR Green Master Mix (Thermo Fisher) on a 7500 Fast Real-Time PCR System (Applied Biosystems) following the manufactures' instructions. The C_t was measured during the exponential amplification phase, and the amplification plots were analyzed using the software v2.0.6 (Applied Biosystems). Relative fold changes were determined by comparative threshold ($\Delta\Delta C_T$) method using *β-actin/RPL19* genes as endogenous normalization control (Livak & Schmittgen, 2001). Data are presented as mean ± SD of three independent experiments, performed in triplicate. Specific primers employed in RT-qPCR amplifications are listed in Table EV1.

Proximity ligation assay (PLA)

Cells were centrifuged mounted on glass slides using a Thermo Shandon Cytospin 2 (Thermo Fisher Scientific) and fixed in 4% formaldehyde for 10 min and permeabilized with 0.1% Triton X-100 in PBS for 5 min at room temperature. *In situ* proximity ligation assay (PLA) was performed using the Duolink InSitu Reagents (Sigma-Aldrich) according to the manufacturer's instructions. The images were captured and analyzed by Zeiss LSM 880 with Airy scan confocal laser scanning microscope by 63X/1.23 NA oil immersion objectives. Six hundred and seventy newton meters of lasers were used to excite the fluorophores. The Zeiss Zen control software (Zeiss, Germany) was used for image analysis.

Mass-spectrometry (MS)

Mass-spectrometry (MS) analysis was performed immunoprecipitating Che-1 from total extracts of Kms27 MM cells. Immunoprecipitation with normal IgG was performed as negative control. Co-Immunoprecipitated complexes were eluted by incubation in 5% SDS in PBS at 95°C and stored at −80°C prior LC–MS analysis. MS processing was performed as previously described (Sorino *et al*, 2020). Results are showed in Dataset EV1.

RNA immunoprecipitation (RIP) with crosslinking

Cells were crosslinked with formaldehyde (F.A.) solution (50 mM HEPES-KOH pH 7.5, 100 mM NaCl, 1 mM EDTA, 0.5 mM EGTA, 11% formaldehyde, ddH_2O) 1% final concentration, 10 min, RT. Nuclei were isolated and resuspended in lysis buffer (Tris–HCl pH 7.5 50 mM, EDTA 1 mM, SDS 0.5%, DTT 1 mM), using 200 µl for each IP sample, and sonicated to obtain a smear not higher than 500 bp. Lysate was treated with DNase (DNAfree, Ambion) and diluted with 400 µl of correction buffer (NP-40, 0.625%, DOC, 0.312%, $MgCl_2$, 5.6 mM, Tris–HCl pH 7.5, 47.5 mM, NaCl, 187.5 mM, glycerol, 12.5%, DTT 1 mM). IP was carried out overnight at +4°C with Che-1/AATF (Bethyl) or S9.6 (Kerafast) antibodies, while normal mouse IgG (Bethyl) functioned as a negative control. IP washing and proteinase K digestion were carried out as above, crosslinking was reversed by incubation at 70°C for 30 min, and RNA was recovered by TRIzol extraction. Immunoprecipitated RNA was tested by RT-qPCR analysis to verify the presence of lncNEAT1 using specific primers (Table EV1) and were calculated by standard curve method and fold of enrichment over IgG.

FISH

Cy5-labeled probes for human NEAT1 (Stellaris RNA Biosearch Techonologies) were used for FISH experiments. For co-localization experiments, we follow the protocol for IF+FISH in Suspension Cells with minor modification. After the permeabilization, we blocked the cytocentrifuge with BSA 5% in PBS 1x for 1 h, followed by a wash in PBS 1x for 10 min, then we proceeded in according with manufacture's protocol. The images were captured and analyzed by Zeiss LSM 880 with Airy scan confocal laser scanning microscope by 63X/1.23 NA oil immersion objectives. Lasers 670 nm were used to excite the fluorophores. The Zeiss Zen control software (Zeiss, Germany) was used for image analysis.

Immunofluorescence

Cytocentrifuged cells were fixed in 4% formaldehyde for 10 min and then permeabilized with 0.1% Triton X-100 in phosphate-buffered saline (PBS) for 5 min at room temperature. Cells were subsequently stained for 2 h with primary antibodies, after which they were rinsed three-times with PBS and stained for 45 min with Alexa-Fluor-594- and Alexa-Fluor-488-conjugated anti-rabbit or anti-mouse secondary antibodies (Thermo Fisher Scientific). Nuclei were visualized by staining with 1 µg/ml Hoechst dye 33,258 (Sigma-Aldrich).

For DNA–RNA hybrids staining, cells were cytocentrifuge and then fixed in ice-cold methanol for 10 min at −20°C. The slides

 © 2022 The Authors

were then quickly washed in PBS 1× and incubated for 1 h in PBS 1× 3% BSA to prevent unspecific interaction. Primary antibody S9.6 was incubated for 2 h at room temperature (RT) in the dark. After three washes with PBS 1× the slides were incubated at RT with secondary anti mouse antibodies. Slides were then washed with PBS 1× and mounted using Duo link in situ mounting medium with DAPI (Sigma). Quantification of the hybrids signal intensity per cell were performed by counting 100 cells per condition in each experiment and analysis were made using ImageJ software.

RNase inhibitors treatments

For IF experiments, cells were cytocentrifuged and permeabilized with PBS 1× plus 0.5% Tween 20 for 5 min at RT. Cells were then treated with 10 U of RNase H (NEB), in PBS 1× for 1 h at RT. For Dot Blot and DRIP seq experiments, RNase H treatments were performed on genomic DNA with 10 U of the enzyme for 1 h at 37°C. Enzymatic treatments with RNase T1 (10 U) and RNase III (5 U) were performed in staining buffer (TBST with 0.1% BSA) as described in Smolka *et al* (2021).

Dot Blot

Genomic DNA was extracted according to DRIP protocol. Serial dilutions of DNA were double spotted on a nitrocellulose membrane and crosslinked with UV light (700 mJ/cm^2). One part of the membrane was blocked with TBS-Tween 0.1 and 5% nonfat dry milk (NFDM) for 1 h and then incubated with S9.6 antibody diluted to 0.5 μg/ml in TBS-Tween plus 2% NFDM. After washing, membrane was incubated with anti-mouse secondary antibodies, further washed, and developed with ECL techniques. The other part of membrane was incubated with Methylene Blue (Sigma M4159 0.2% (w/v) in 0.4 M sodium acetate:0.4 M acetic acid) for 15 min, as loading control, and at the end of the incubation washed with water. Both the membranes were acquired and quantified using Alliance Mini HD6 system by UVITEC Ltd, Cambridge, equipped with UVI1D Software (UVITEC, 14–630,275).

ChIP-seq

ChIP-seq experiments were performed following ChIPmentation protocol (Bruno *et al*, 2020) in duplicate for Che-1/AATF. The final libraries were controlled on an Agilent 2100 Bioanalyzer (Agilent Technologies) and sequenced on a NextSeq 500 (Illumina, CA) using 50 cycles single-end mode.

RNA-Seq

Total RNA was extracted from the same number of viable cells using QIAzol Lysis Reagent (Qiagen). ExFold RNA Spike-In Mixes (ERCC, Thermo Fisher Scientific) were added to each sample for normalizing gene expression. RNA libraries for sequencing were generated in triplicate by using the same amount of RNA for each sample according to the Illumina TruSeq Stranded Total RNA kit with an initial ribosomal depletion step using Ribo Zero Gold (Illumina, CA). The libraries were quantified by RT-qPCR and sequenced in paired-end mode (2 × 75 bp) with NextSeq 500 (Illumina, CA).

ChIRP-seq

ChIRP was performed as described (Chu *et al*, 2012). Twenty million cells were used for each condition. The oligonucleotides used for NEAT1 immunoprecipitation are listed in Table EV1. Biotinylated oligonucleotides were recovered using Dynabeads® MyOne™ Streptavidin C1 (Invitrogen). After the washing steps, all the recovered material was used for DNA purification and subsequently utilized for the construction of the library by Accel-NGS 2S Plus DNA library kits (Swift Biosciences) according to the manufacturer's instructions.

DRIP-seq

DRIP-seq assays were performed as previously described (Ginno *et al*, 2012). Briefly, nucleic acids were extracted from Kms27 MM cells by SDS/proteinase K treatment at 37°C overnight followed by phenol–chloroform isoamyl extraction and ethanol precipitation at room temperature. The harvested nucleic acids were digested for 24 h at 37°C using a restriction enzyme cocktail (50 units/100 μg nucleic acids, each of BsrGI, EcoRI, HindIII, SspI, and XbaI) in the New England Biolabs CutSmart buffer with 2 mM Spermidine and 1× BSA. Digested DNAs were cleaned up by phenol–chloroform isoamyl extraction followed by treated with RNase H (10 units/100 μg nucleic acids) overnight at 37°C in the New England Biolabs RNase H buffer. DNA/RNA hybrids from 4.0 μg digested nucleic acids, treated or not with RNase H, were immunoprecipitated using 5 μg of S9.6 antibody (Kerafast) and 20 μl of Protein G Dynabeads (Thermo Fisher) at 4°C overnight in IP buffer (10 mM $NaPO_4$, 140 mM NaCl, and 0.05% Triton X-100). The beads were then washed four times with IP buffer for 10 min at room temperature, and the nucleic acids were eluted with elution buffer (50 mM Tris–HCl, pH 8.0, 10 mM EDTA, 0.5% SDS, and 70 μg of protease K) at 55°C for 1 h. Immunoprecipitated DNA was then cleaned up by a phenol–chloroform extraction followed by ethanol precipitation at −20°C for 1 h. The quantity of the immunoprecipitated material was determined by Qubit 2.0 fluorometer (Life Technologies). About 10 ng of the immunoprecipitated DNA was used to prepare the libraries for sequencing by following the manufacturer's instructions including DNA and repairing, adaptor ligation, and amplification (Illumina, CA). The libraries were then sequenced using the NextSeq 500 system (Illumina, CA).

Statistical analysis

Data are presented as mean of three independent experiments ± SD. Statistical analyses were performed using R software. Two-tailed Student's *t*-tests with Benjamini–Hochberg correction were performed to compare one parameter between two groups. Statistical significance is indicated by asterisks as follows: $*P < 0.05$, $**P < 0.01$, $***P < 0.005$, $****P < 0.001$, n.s. = not significant.

Computational methods

ChIRP-seq and ChIP-seq data processing

Reads of each experiment were quality controlled with FASTQC v0.11.9 (http://www.bioinformatics.babraham.ac.uk/projects/fastqc/) combined with MultiQC v.1.9 (Ewels *et al*, 2016) and aligned to the reference genome hg19 using bowtie2 (Langmead & Salzberg, 2012) v.2.3.5.1 setting—local mode with default parameters. The generated sequence alignments were stored into SAM format files and converted into BAM format, sorted, and indexed with SAMtools (Li *et al*, 2009) v.1.2. The duplicated reads were removed by utilizing MarkDuplicated tool available in GATK4 suite v.4.1.8.1. Peaks were called using the function callpeak of MACS2 v.2.2.6 tool (parameters: --format AUTO --broad -B -q 0.1 -g hs), and those

© 2022 The Authors

matching backlisted regions of hg19 were removed. Peaks stored in bedGraph format files were sorted and converted in bigWig format with bedGraphToBigWig (Kent *et al*, 2010) v.4. Significant signals were annotated by using the function annotatePeaks.pl of HOMER (Heinz *et al*, 2010) v.4.11 tool.

Heatmap and enrichment profiles of ChIRP-seq, ChIP-seq, DRIP-seq profiles

Heatmap profiles were obtained by using the function included in DeepTools v.3.5.0 computeMatrix (parameters: scale-regions -a 5,000 -b 5,000—region Body Length 5,000–skipZeros—missingDataAsZero) and plotHeatmap (parameters: sortRegions descend —sortUsing max—colorMap OrRd—zMin 0—zMax 15—dpi 300), respectively. Visualization of peak profiles were obtained using bigwig files of each experiment provided as input to Integrative Genomics Viewer (IGV).

NEAT1 and Che-1 co-localization identification

The identification of the co-localizing sites between Che-1 and NEAT1 relies on a multistep process which include the generation of a master list using TSSs coordinates reported in the Ensembl release 103 (Yates *et al*, 2020) and referred to the GRCh37 reference genome. The master list was obtained using the biomart tool available on the Ensembl website and refined by removing mitochondrial coordinates and patches. A total of 92.226 TSSs were retained in the final master list. Each set of coordinates was extended by 2 kb, both upstream and downstream. The master list was populated at each TSS site with Che-1, and NEAT1 read enrichment computed by using the multicov function of bedtools v2.29.2 tool and using ChIRP-seq and ChIP-seq deduplicated bam files as input. The obtained reads counts were quantile normalized after log2-counts per million transformation with the function voom of LIMMA (Ramirez *et al*, 2014) v3.44.3 package in R.

The identification of Che-1 and NEAT1 co-localized signal was obtained by using read enrichment cut-offs independently as follows: (i) The normalized reads count assigned to each TSS of both experiments were used to determine two independent series of cut-offs by dividing each distribution of normalized read counts in 15 quantile sections. (ii) Iteratively, our algorithm scans each peak from the 1^{st} (lowest enriched) quantile to the 15^{th} quantile (top enriched) in incremental order. Each iteration includes the peaks being part of the previous quantiles. At each iteration assigns a value of 1 to the peak included in the quantile group, and a value of 0 in the case is not called. A signal is considered co-localized when in both experiments, the assigned value is 1. Each iteration is concluded with the calculation of a Jaccard coefficient score. (iii) The number of co-localizing sites and Jaccard score obtained from each iteration were independently plotted with an in-house R script. The intersection of the two lines was considered the point of threshold for co-occurrence selection. The point of intersection corresponded to the 11^{th} iteration.

RBPs binding to NEAT-1-protein analysis

BednarrowPeak and *bigWig* files of 120 RBPs eCLIP profiles generated from K562 cell line and aligned to HG19 reference genome were downloaded from Encode Project database (v113). Peaks intersecting the NEAT1 domains (left domain: chr11:65190234–65198234; central domain: chr11:65198234–65206834; right domain: chr11:65206834–652129) (PMID: 29932899) with a length greater than 500 bps were retained for further analysis. The classification of peaks was plotted by using ggplot2[8] R package.

DRIP-seq data processing

DRIP-seq data were quality checked by using FASTQC v0.11.91, forwarded to bowtie23 v.2.3.5.1(parameters: -p 6 -t --local) and aligned to the reference genome hg19 and GRCh38. The alignments were saved in SAM format files and converted into BAM format which were subsequently sorted and indexed by using SAMtools4 v.1.2. Peaks were called with the function callpeak of MACS2 v.2.2.6 tools (parameters: --broad --format AUTO -B -q 0.01) and after sorting, were converted from bedGraph to BigWig format by using bedGraphToBigWig (Kent *et al*, 2010) v.4 tool. RNAse H-treated sample bam file was used as input in the peak calling process. A series of Deeptools v.3.5.0 functions including computeMatrix (parameters: referece-point -p 6 -a 1,500 -b 1,500 --regionBodyLength 1,500), plotProfile (parameters: plotHeight 10 –plotWidth 20 –dpi 300) and plotHeatmap (parameters: sortRegions descend—sortUsing max—colorMap coolwarm—zMin 0—zMax 55—dpi 300—heatmapHeight 15—heatmapWidth 28) were used to visualize the enrichment at the ribosomal sites in DRIP-seq data. The inputs were the BigWig files and the list of ribosomal subunits coordinates based on GRCh38 genome annotation. Furthermore, the corresponding peaks profiles were displayed by using the BigWig of DRIP-seq samples as inputs to IGV tool.

RNA-seq analysis

NEAT1 q vs. GapmeR NEAT-1 RNA-seq and Che1 vs. siChe-1 RNA-seq were independently analyzed by using the Kallisto v.0.46.0(Bray *et al*, 2016) and Sleuth v.0.30.0 (Pimentel *et al*, 2017) pipeline. Sequencing quality of each sample was assessed with FASTQC v0.11.91 and summarized with MultiQC v.1.92. Read quantification was performed with the function quant of Kallisto tool (parameters: -b 100). The pseudoalignment was executed against the reference genome GRCh37 downloaded from NCBI and subsequently indexed with the function index available in Kallisto.

The Kallisto results were processed and normalized through the function sleuth_prep with gene-level resolution (parameters: extra_bootstrap_summary = T, gene_mode = TRUE). The gene-transcripts correspondence map was retrieved through the functions useMart and getBM of biomaRT R package (Durinck *et al*, 2009). Those correspondences were annotated based on grch37 of Ensembl release 103(Yates *et al*, 2020). Differential analysis was conducted by fitting full and reduced models through the function sleuth_fit with the formula parameter, respectively, set to full and reduced. The processed reads counts were converted in transcript per million measurements through the function sleuth_to_matrix of Sleuth (Pimentel *et al*, 2017) R package.

Principal component analysis (PCA) was executed pre- and post-normalization. Prenormalized PCA was executed using the function prcomp of stats v.4.0.2 R package (http://www.r-project.org/index.html) and plotted through the function autoplot of ggfortify v.0.4.11 R package. Postnormalized PCA was carried out with the function plot_pca of Sleuth (Pimentel *et al*, 2017) package in R.

Wald test was performed with the function sleuth_wt of Sleuth (Pimentel *et al*, 2017) R package. The beta-value and *q*-value obtained from the test were used to discriminate between genes

© 2022 The Authors

significantly up ($b > 0.7$ and q-value < 0.05) or down ($b < -0.7$ and q-value < 0.05) regulated.

Functional enrichment analysis of differential expressed genes (DEGs) was executed through GSEA online portal released in July 2020 (http://www.gsea-msigdb.org) by interrogating the MSigDB Hallmarks collection. Pathway's perturbation analysis was performed by running PROGENy (Schubert *et al*, 2018) v.1.10.0 R package providing RNA-seq data as input.

Transcriptome analysis of the CoMMpass dataset

Raw gene counts of CoMMpass dataset (IA15 release) were downloaded from the MMREF Research Gateway Portal, table name MMRF_CoMMpass_IA14a_E74GTF_Salmon_Gene_Counts. We selected a cohort of 687 samples having assigned the relative ISS score and the transcriptome. Gene counts of selected samples were normalized through a multistep workflow using edgeR (Robinson *et al*, 2010) functions as follows DGEList, estimateCommonDisp, estimateTaqwiseDisp, calcNormFactors with TMM method. The normalized matrix was populated with the cpm value to each gene within every patient. To identify genes differentially transcribed between ISS scores we iteratively screened each gene and then computing the Mann–Whitney test for each ISS combination providing the relative cpm value for each patient. Only genes differentially enriched (P-value < 0.05) in at least one ISS combination were retained in the final matrix for further use.

Enrichment of paraspeckles genes in disease progression

Paraspeckles genes (Fox *et al*, 2018) (*NEAT1*, *AATF*, *NONO*, *HNRNPK*, *DAZAP1*, *HNRNPH3*, *SRSF1*, *SFPQ*, *FUS*, *RBM14*, *TAF15*) were selected from the normalized matrix and plotted by the relative ISS score associated to each patient through ggpubr R package.

IFN gene signature analysis

We investigated the expression of genes associated to the interferon gamma (IFNG) and interferon alpha (IFNA) pathway. We generated a customized list of 198 IFN genes which were collected from *Reactome*, *Signal Transduction Knowledge Environment*, *Biocarta*, *WikiPathways* stored in GSEA website (https://www.gsea-msigdb.org/gsea/msigdb/search.jsp) in January 2021. Only IFN genes significantly up-regulated between the cohort of patients at ISS-1 and ISS-3 were retained for further analysis. A gene was considered significantly up regulated if the P-value obtained from the Mann–Whitney test was lower than 0.05 and the median cpm value of the whole cohort at ISS-3 was higher than ISS-1. The final selected IFN signature was composed by 29 genes which were consistently upregulated at ISS-3 compared ISS-1 and were used in the further analyses.

IFN score assignment

An IFN score was assigned to each patient in the CoMMpass cohort. IFN score ranges from 1 to 3, that is, 1 = low,2 = medium, 3 = high IFN genes expression. To define the IFN score we (1) calculated the value of the third quartile of each normalized gene count distribution within the CoMMpass cohort ($N = 687$) as independent cut-off for defining a gene as highly expressed. A patient was considered a high expressor of a gene when the relative gene expression was beyond the third quartile enrichment. Patients exhibiting <5 gene highly expressed were included in the IFN low group, those exhibiting between 5 and 13 genes were assigned to the IFN medium and those with more than 13 genes assigned to IFN high group. The frequency of patients in each group was plotted by the relative ISS with an in-house R script.

Survival analysis

Two different survival analyses were conducted to reveal the role of IFN pathway in the MM disease progression. The overall survival (OS) information for the analysis was retrieved from table named "MMRF_CoMMpass_IA15_STAND_ALONE_SURVIVAL.csv" stored on MMREF Research Gateway Portal. Patients with OS greater than 65 months were excluded ($n = 56$) from the analysis. Survival curves were estimated with the Kaplan–Meier product-limit method and compared by log-rank test. Univariate Cox regression analyses were carried out to identify potential predictors of survival.

The first survival curve examines the group of patients exhibiting high IFN score ($n = 71$) versus the patients assigned to low and medium IFN score groups ($n = 614$), defined as described above.

The second survival curve examine two groups of patients of similar size (IFN-low:341 vs. IFN-high: 291). Patients were ranked based on the number of highly expressed gene involved in IFN pathway. Then, the median value of the ranking was set as threshold to divide the population in high vs. low IFN signature.

Both survival analyses were carried out by using survfit and Surv functions in survival v.3.1.12 R package. The Kaplan–Meier curves were generated by utilizing the function ggsurvplot of survminer v.0.4.819 R package and both of them had significance equal to log-rank P-value < 0.001.

Multivariate analysis

The patients used for the survival analysis were classified according to: type of therapy (V-based, K-based, combo K/IMIDs-based, combo V/IMIDs/K-based, combo IMIDs/K-based, IMIDs-based), autologous stem-cell transplantation (ASCT; yes/no), presence or absence of translocations and copy-number abnormalities (CNAs). The definition of variables is accurately described in Appendix Table S1. The translocations taken into consideration were those occurring at IgH and IgL locus (Barwick *et al*, 2019) [t(11;14), t(4;14), t(14;16), t(4;20)] specifically found in MM disease, and were evaluated using calls on WGS long-insert data downloaded from MMREF Research Gateway Portal, table name MMRF_CoMMpass_IA15a_LongInsert_Canonical_Ig_Translocations. Nonsynonymous alterations occurring in a customized set of 21 genes (Bolli *et al*, 2014) knowing to be mutated in MM were evaluated utilizing WGS long-insert data downloaded from MMREF Research Gateway Portal, table name MMRF_CoMMpass_IA15a_All_Canonical_NS_Variants_ENSG_Mutation_Counts.

Univariate Cox analysis of time to death was performed for each variable in the Tables EV2–EV5 by using the functions coxph and Surv of survival v.3.1.12 R package. Those variables resulted significant (P-value ≤ 0.06) at univariate analysis (IFN, ASCT, ISS, Therapy, KRAS, TP53, LTB, FGFR3) and two translocations essential in MM (MYC-translocation, CCND1-translocation) were used to carry out the multivariate Cox analysis of time to death. The statistical results were reported in Tables EV2–EV5. We fitted multivariate analyses by utilizing the functions coxph and Surv of survival v.3.1.12 R package with parameter na.action set to na.exclude. The multivariate analysis results were visualized with the function ggforest of survminer v.0.4.8 R package.

© 2022 The Authors

Data Availability

The mass spectrometry data (Raw data and MaxQuant output) have been deposited to the Proteome Xchange Consortium via the PRIDE partner repository with the dataset identifier PXD026659 (https://www.ebi.ac.uk/pride/archive/projects/PXD026659/). High Throughput Sequencing data (RNA-seq, ChIP-seq, ChIRP-seq, DRIP-seq) from this publication have been submitted to the National Cancer Center for Biotechnology Information (NCBI) Gene Expression Omnibus database and assigned the identifier numbers GSE178868 (https://www.ncbi.nlm.nih.gov/geo/query/acc.cgi?acc=GSE178868). The full resolution microscope images have been deposited to the GARRbox data storage and are available at the following link: https://gbox.garr.it/garrbox/index.php/s/HD04TFXAGEyiSpG. All other data supporting the findings of this study are available from the corresponding authors on reasonable request.

Expanded View for this article is available online.

Acknowledgments
The authors thank all patients and their families for the support and for donating the research samples. They thank Stefano Scalera and Marcello Maugeri-Saccà for the technical assistance in supervising the survival analysis. These data were generated as part of the Multiple Myeloma Research Foundation Personalized Medicine Initiatives (https://research.themmrf.org and www.themmrf.org). This work was supported by the Italian Association for Cancer Research (A.I.R.C.) 15255 and Italian Ministry of Health (RF-2019-12368737 and Current Research). G. Corleone has received funding from AIRC and from the European Union's Horizon 2020 research and innovation program under the Marie Skłodowska-Curie grant agreement No. 800924.

Author contributions
Tiziana Bruno: Validation; investigation; visualization; methodology; writing – original draft; writing – review and editing. **Giacomo Corleone:** Data curation; formal analysis; validation; visualization; methodology; writing – original draft; writing – review and editing. **Valeria Catena:** Validation; investigation; visualization; writing – review and editing. **Clelia Cortile:** Formal analysis; visualization. **Francesca De Nicola:** Investigation. **Francesca Fabretti:** Formal analysis; investigation. **Svitlana Gumenyuk:** Resources. **Francesco Pisani:** Resources. **Andrea Mengarelli:** Resources. **Claudio Passananti:** Conceptualization. **Maurizio Fanciulli:** Conceptualization; data curation; supervision; funding acquisition; writing – original draft; project administration; writing – review and editing.

Disclosure and Competing Interests Statement
The authors declare that they have no conflict of interest.

References

Abraham KJ, Khosraviani N, Chan JNY, Gorthi A, Samman A, Zhao DY, Wang M, Bokros M, Vidya E, Ostrowski LA *et al* (2020) Nucleolar RNA polymerase II drives ribosome biogenesis. *Nature* 585: 298 – 302

Agnelli L, Mosca L, Fabris S, Lionetti M, Andronache A, Kwee I, Todoerti K, Verdelli D, Battaglia C, Bertoni F *et al* (2009) A SNP microarray and FISH-based procedure to detect allelic imbalances in multiple myeloma: an integrated genomics approach reveals a wide gene dosage effect. *Genes Chromosomes Cancer* 48: 603 – 614

Bammert L, Jonas S, Ungricht R, Kutay U (2016) Human AATF/Che-1 forms a nucleolar protein complex with NGDN and NOL10 required for 40S ribosomal subunit synthesis. *Nucleic Acids Res* 44: 9803 – 9820

Barwick BG, Neri P, Bahlis NJ, Nooka AK, Dhodapkar MV, Jaye DL, Hofmeister CC, Kaufman JL, Gupta VA, Auclair D *et al* (2019) Multiple myeloma immunoglobulin lambda translocations portend poor prognosis. *Nat Commun* 10: 1911

Belotserkovskii BP, Tornaletti S, D'Souza AD, Hanawalt PC (2018) R-loop generation during transcription: Formation, processing and cellular outcomes. *DNA Repair (Amst)* 71: 69 – 81

Boguslawski SJ, Smith DE, Michalak MA, Mickelson KE, Yehle CO, Patterson WL, Carrico RJ (1986) Characterization of monoclonal antibody to DNA.RNA and its application to immunodetection of hybrids. *J Immunol Methods* 89: 123 – 130

Bolli N, Avet-Loiseau H, Wedge DC, Van Loo P, Alexandrov LB, Martincorena I, Dawson KJ, Iorio F, Nik-Zainal S, Bignell GR *et al* (2014) Heterogeneity of genomic evolution and mutational profiles in multiple myeloma. *Nat Commun* 5: 2997

Bray NL, Pimentel H, Melsted P, Pachter L (2016) Near-optimal probabilistic RNA-seq quantification. *Nat Biotechnol* 34: 525 – 527

Bruno T, Desantis A, Bossi G, Di Agostino S, Sorino C, De Nicola F, Iezzi S, Franchitto A, Benassi B, Galanti S *et al* (2010) Che-1 promotes tumor cell survival by sustaining mutant p53 transcription and inhibiting DNA damage response activation. *Cancer Cell* 18: 122 – 134

Bruno T, De Nicola F, Corleone G, Catena V, Goeman F, Pallocca M, Sorino C, Bossi G, Amadio B, Cigliana G *et al* (2020) Che-1/AATF-induced transcriptionally active chromatin promotes cell proliferation in multiple myeloma. *Blood Adv* 4: 5616 – 5630

Chakraborty P, Huang JTJ, Hiom K (2018) DHX9 helicase promotes R-loop formation in cells with impaired RNA splicing. *Nat Commun* 9: 4346

Choo J, Schlosser D, Manzini V, Magerhans A, Dobbelstein M (2020) The integrated stress response induces R-loops and hinders replication fork progression. *Cell Death Dis* 11: 538

Chu C, Quinn J, Chang HY (2012) Chromatin isolation by RNA purification (ChIRP). *J Vis Exp* 3912 https://doi.org/10.3791/3912

Clemson CM, Hutchinson JN, Sara SA, Ensminger AW, Fox AH, Chess A, Lawrence JB (2009) An architectural role for a nuclear noncoding RNA: NEAT1 RNA is essential for the structure of paraspeckles. *Mol Cell* 33: 717 – 726

Cottini F, Hideshima T, Suzuki R, Tai YT, Bianchini G, Richardson PG, Anderson KC, Tonon G (2015) Synthetic lethal approaches exploiting DNA damage in aggressive myeloma. *Cancer Discov* 5: 972 – 987

Cristini A, Groh M, Kristiansen MS, Gromak N (2018) RNA/DNA hybrid interactome identifies DXH9 as a molecular player in transcriptional termination and R-loop-associated DNA damage. *Cell Rep* 23: 1891 – 1905

Desantis A, Bruno T, Catena V, De Nicola F, Goeman F, Iezzi S, Sorino C, Ponzoni M, Bossi G, Federico V *et al* (2015) Che-1-induced inhibition of mTOR pathway enables stress-induced autophagy. *EMBO J* 34: 1214 – 1230

Durinck S, Spellman PT, Birney E, Huber W (2009) Mapping identifiers for the integration of genomic datasets with the R/Bioconductor package biomaRt. *Nat Protoc* 4: 1184 – 1191

Dutrieux L, Lin YL, Lutzmann M, Rodriguez R, Cogne M, Pasero P, Moreaux J (2021) Transcription/replication conflicts in tumorigenesis and their potential role as novel therapeutic targets in multiple myeloma. *Cancers (Basel)* 13: 3755

Espin-Palazon R, Weijts B, Mulero V, Traver D (2018) Proinflammatory signals as fuel for the fire of hematopoietic stem cell emergence. *Trends Cell Biol* 28: 58 – 66

 © 2022 The Authors

Ewels P, Magnusson M, Lundin S, Kaller M (2016) MultiQC: summarize analysis results for multiple tools and samples in a single report. *Bioinformatics* 32: 3047 – 3048

Fanciulli M, Bruno T, Di Padova M, De Angelis R, Iezzi S, Iacobini C, Floridi A, Passananti C (2000) Identification of a novel partner of RNA polymerase II subunit 11, Che-1, which interacts with and affects the growth suppression function of Rb. *FASEB J* 14: 904 – 912

Ferraris SE, Isoniemi K, Torvaldson E, Anckar J, Westermarck J, Eriksson JE (2012) Nucleolar AATF regulates c-Jun-mediated apoptosis. *Mol Biol Cell* 23: 4323 – 4332

Folgiero V, Sorino C, Pallocca M, De Nicola F, Goeman F, Bertaina V, Strocchio L, Romania P, Pitisci A, Iezzi S *et al* (2018) Che-1 is targeted by c-Myc to sustain proliferation in pre-B-cell acute lymphoblastic leukemia. *EMBO Rep* 19: e44871

Fox AH, Lamond AI (2010) Paraspeckles. *Cold Spring Harb Perspect Biol* 2: a000687

Fox AH, Nakagawa S, Hirose T, Bond CS (2018) Paraspeckles: where long noncoding RNA meets phase separation. *Trends Biochem Sci* 43: 124 – 135

Garcia-Muse T, Aguilera A (2019) R loops: from physiological to pathological roles. *Cell* 179: 604 – 618

Ginno PA, Lott PL, Christensen HC, Korf I, Chedin F (2012) R-loop formation is a distinctive characteristic of unmethylated human CpG Island promoters. *Mol Cell* 45: 814 – 825

Groh M, Gromak N (2014) Out of balance: R-loops in human disease. *PLoS Genet* 10: e1004630

Hanamura I, Huang Y, Zhan F, Barlogie B, Shaughnessy J (2006) Prognostic value of cyclin D2 mRNA expression in newly diagnosed multiple myeloma treated with high-dose chemotherapy and tandem autologous stem cell transplantations. *Leukemia* 20: 1288 – 1290

Heinz S, Benner C, Spann N, Bertolino E, Lin YC, Laslo P, Cheng JX, Murre C, Singh H, Glass CK (2010) Simple combinations of lineage-determining transcription factors prime cis-regulatory elements required for macrophage and B cell identities. *Mol Cell* 38: 576 – 589

Hirose T, Virnicchi G, Tanigawa A, Naganuma T, Li R, Kimura H, Yokoi T, Nakagawa S, Benard M, Fox AH *et al* (2014) NEAT1 long noncoding RNA regulates transcription via protein sequestration within subnuclear bodies. *Mol Biol Cell* 25: 169 – 183

Hopfner KP, Hornung V (2020) Molecular mechanisms and cellular functions of cGAS-STING signalling. *Nat Rev Mol Cell Biol* 21: 501 – 521

Huang HH, Ferguson ID, Thornton AM, Bastola P, Lam C, Lin YT, Choudhry P, Mariano MC, Marcoulis MD, Teo CF *et al* (2020) Proteasome inhibitor-induced modulation reveals the spliceosome as a specific therapeutic vulnerability in multiple myeloma. *Nat Commun* 11: 1931

Iezzi S, Fanciulli M (2015) Discovering Che-1/AATF: a new attractive target for cancer therapy. *Front Genet* 6: 141

Jing P, Zou J, Weng K, Peng P (2018) The PI3K/AKT axis modulates AATF activity in Wilms' tumor cells. *FEBS Open Bio* 8: 1615 – 1623

Kaiser RWJ, Ignarski M, Van Nostrand EL, Frese CK, Jain M, Cukoski S, Heinen H, Schaechter M, Seufert L, Bunte K *et al* (2019) A protein-RNA interaction atlas of the ribosome biogenesis factor AATF. *Sci Rep* 9: 11071

Kent WJ, Zweig AS, Barber G, Hinrichs AS, Karolchik D (2010) BigWig and BigBed: enabling browsing of large distributed datasets. *Bioinformatics* 26: 2204 – 2207

Kumar SK, Rajkumar V, Kyle RA, van Duin M, Sonneveld P, Mateos MV, Gay F, Anderson KC (2017) Multiple myeloma. *Nat Rev Dis Primers* 3: 17046

Kumar DP, Santhekadur PK, Seneshaw M, Mirshahi F, Uram-Tuculescu C, Sanyal AJ (2019) A regulatory role of apoptosis antagonizing transcription factor in the pathogenesis of nonalcoholic fatty liver disease and hepatocellular carcinoma. *Hepatology* 69: 1520 – 1534

Langmead B, Salzberg SL (2012) Fast gapped-read alignment with Bowtie 2. *Nat Methods* 9: 357 – 359

Li H, Handsaker B, Wysoker A, Fennell T, Ruan J, Homer N, Marth G, Abecasis G, Durbin R, 1000 Genome Project Data Processing Subgroup (2009) The Sequence Alignment/Map format and SAMtools. *Bioinformatics* 25: 2078 – 2079

Lim YW, Sanz LA, Xu X, Hartono SR, Chedin F (2015) Genome-wide DNA hypomethylation and RNA:DNA hybrid accumulation in Aicardi-Goutieres syndrome. *Elife* 4: e08007

Liu X, Cai S, Zhang C, Liu Z, Luo J, Xing B, Du X (2018) Deacetylation of NAT10 by Sirt1 promotes the transition from rRNA biogenesis to autophagy upon energy stress. *Nucleic Acids Res* 46: 9601 – 9616

Livak KJ, Schmittgen TD (2001) Analysis of relative gene expression data using real-time quantitative PCR and the 2(-Delta Delta C(T)) Method. *Methods* 25: 402 – 408

Manier S, Salem K, Glavey SV, Roccaro AM, Ghobrial IM (2016) Genomic aberrations in multiple myeloma. *Cancer Treat Res* 169: 23 – 34

Manier S, Salem KZ, Park J, Landau DA, Getz G, Ghobrial IM (2017) Genomic complexity of multiple myeloma and its clinical implications. *Nat Rev Clin Oncol* 14: 100 – 113

Motwani M, Pesiridis S, Fitzgerald KA (2019) DNA sensing by the cGAS-STING pathway in health and disease. *Nat Rev Genet* 20: 657 – 674

Neuse CJ, Lomas OC, Schliemann C, Shen YJ, Manier S, Bustoros M, Ghobrial IM (2020) Genome instability in multiple myeloma. *Leukemia* 34: 2887 – 2897

Nikesitch N, Lee JM, Ling S, Roberts TL (2018) Endoplasmic reticulum stress in the development of multiple myeloma and drug resistance. *Clin Transl Immunology* 7: e1007

Nolan GP, Ghosh S, Liou HC, Tempst P, Baltimore D (1991) DNA binding and I kappa B inhibition of the cloned p65 subunit of NF-kappa B, a rel-related polypeptide. *Cell* 64: 961 – 969

Petti E, Buemi V, Zappone A, Schillaci O, Broccia PV, Dinami R, Matteoni S, Benetti R, Schoeftner S (2019) SFPQ and NONO suppress RNA:DNA-hybrid-related telomere instability. *Nat Commun* 10: 1001

Pietras EM (2017) Inflammation: a key regulator of hematopoietic stem cell fate in health and disease. *Blood* 130: 1693 – 1698

Pimentel H, Bray NL, Puente S, Melsted P, Pachter L (2017) Differential analysis of RNA-seq incorporating quantification uncertainty. *Nat Methods* 14: 687 – 690

Pineiro D, Stoneley M, Ramakrishna M, Alexandrova J, Dezi V, Juke-Jones R, Lilley KS, Cain K, Willis AE (2018) Identification of the RNA polymerase I-RNA interactome. *Nucleic Acids Res* 46: 11002 – 11013

Ramirez F, Dundar F, Diehl S, Gruning BA, Manke T (2014) deepTools: a flexible platform for exploring deep-sequencing data. *Nucleic Acids Res* 42: W187 – W191

Robinson MD, McCarthy DJ, Smyth GK (2010) edgeR: a Bioconductor package for differential expression analysis of digital gene expression data. *Bioinformatics* 26: 139 – 140

Santos-Pereira JM, Aguilera A (2015) R loops: new modulators of genome dynamics and function. *Nat Rev Genet* 16: 583 – 597

Sanz LA, Hartono SR, Lim YW, Steyaert S, Rajpurkar A, Ginno PA, Xu X, Chedin F (2016) Prevalent, dynamic, and conserved R-loop structures associate with specific epigenomic signatures in mammals. *Mol Cell* 63: 167 – 178

Sawamiphak S, Kontarakis Z, Stainier DY (2014) Interferon gamma signaling positively regulates hematopoietic stem cell emergence. *Dev Cell* 31: 640 – 653

© 2022 The Authors

Schubert M, Klinger B, Klunemann M, Sieber A, Uhlitz F, Sauer S, Garnett MJ, Bluthgen N, Saez-Rodriguez J (2018) Perturbation-response genes reveal signaling footprints in cancer gene expression. *Nat Commun* 9: 20

Shen YJ, Le Bert N, Chitre AA, Koo CX, Nga XH, Ho SS, Khatoo M, Tan NY, Ishii KJ, Gasser S (2015) Genome-derived cytosolic DNA mediates type I interferon-dependent rejection of B cell lymphoma cells. *Cell Rep* 11: 460 – 473

Sidrauski C, Acosta-Alvear D, Khoutorsky A, Vedantham P, Hearn BR, Li H, Gamache K, Gallagher CM, Ang KK, Wilson C *et al* (2013) Pharmacological brake-release of mRNA translation enhances cognitive memory. *Elife* 2: e00498

Smolka JA, Sanz LA, Hartono SR, Chedin F (2021) Recognition of RNA by the S9.6 antibody creates pervasive artifacts when imaging RNA:DNA hybrids. *J Cell Biol* 220: e202004079

Sorino C, Catena V, Bruno T, De Nicola F, Scalera S, Bossi G, Fabretti F, Mano M, De Smaele E, Fanciulli M *et al* (2020) Che-1/AATF binds to RNA polymerase I machinery and sustains ribosomal RNA gene transcription. *Nucleic Acids Res* 48: 5891 – 5906

Taiana E, Ronchetti D, Favasuli V, Todoerti K, Manzoni M, Amodio N, Tassone P, Agnelli L, Neri A (2019) Long non-coding RNA NEAT1 shows high expression unrelated to molecular features and clinical outcome in multiple myeloma. *Haematologica* 104: e72 – e76

Taiana E, Favasuli V, Ronchetti D, Todoerti K, Pelizzoni F, Manzoni M, Barbieri M, Fabris S, Silvestris I, Gallo Cantafio ME *et al* (2020) Long non-coding RNA NEAT1 targeting impairs the DNA repair machinery and triggers anti-tumor activity in multiple myeloma. *Leukemia* 34: 234 – 244

Tsai JC, Miller-Vedam LE, Anand AA, Jaishankar P, Nguyen HC, Renslo AR, Frost A, Walter P (2018) Structure of the nucleotide exchange factor eIF2B reveals mechanism of memory-enhancing molecule. *Science* 359: eaaq0939

Van Nostrand EL, Freese P, Pratt GA, Wang X, Wei X, Xiao R, Blue SM, Chen JY, Cody NAL, Dominguez D *et al* (2020) A large-scale binding and functional map of human RNA-binding proteins. *Nature* 583: 711 – 719

Weinreb JT, Gupta V, Sharvit E, Weil R, Bowman TV (2021) Ddx41 inhibition of DNA damage signaling permits erythroid progenitor expansion in zebrafish. *Haematologica* 107: 644 – 654

Welcker D, Jain M, Khurshid S, Jokic M, Hohne M, Schmitt A, Frommolt P, Niessen CM, Spiro J, Persigehl T *et al* (2018) AATF suppresses apoptosis, promotes proliferation and is critical for Kras-driven lung cancer. *Oncogene* 37: 1503 – 1518

West JA, Davis CP, Sunwoo H, Simon MD, Sadreyev RI, Wang PI, Tolstorukov MY, Kingston RE (2014) The long noncoding RNAs NEAT1 and MALAT1 bind active chromatin sites. *Mol Cell* 55: 791 – 802

Wu T, Nance J, Chu F, Fazzio TG (2021) Characterization of R-loop-interacting proteins in embryonic stem cells reveals roles in rRNA processing and gene expression. *Mol Cell Proteomics* 20: 100142

Yamazaki T, Hirose T (2015) The building process of the functional paraspeckle with long non-coding RNAs. *Front Biosci (Elite Ed)* 7: 1 – 41

Yamazaki T, Souquere S, Chujo T, Kobelke S, Chong YS, Fox AH, Bond CS, Nakagawa S, Pierron G, Hirose T (2018) Functional domains of NEAT1 architectural lncRNA induce paraspeckle assembly through phase separation. *Mol Cell* 70: 1038 – 1053.e7

Yates AD, Achuthan P, Akanni W, Allen J, Allen J, Alvarez-Jarreta J, Amode MR, Armean IM, Azov AG, Bennett R *et al* (2020) Ensembl 2020. *Nucleic Acids Res* 48: D682 – D688

Yoneyama M, Kikuchi M, Natsukawa T, Shinobu N, Imaizumi T, Miyagishi M, Taira K, Akira S, Fujita T (2004) The RNA helicase RIG-I has an essential function in double-stranded RNA-induced innate antiviral responses. *Nat Immunol* 5: 730 – 737

Zyryanova AF, Weis F, Faille A, Alard AA, Crespillo-Casado A, Sekine Y, Harding HP, Allen F, Parts L, Fromont C *et al* (2018) Binding of ISRIB reveals a regulatory site in the nucleotide exchange factor eIF2B. *Science* 359: 1533 – 1536

License: This is an open access article under the terms of the Creative Commons Attribution-NonCommercial-NoDerivs License, which permits use and distribution in any medium, provided the original work is properly cited, the use is non-commercial and no modifications or adaptations are made.